Modeling Dynamic Behavior of Metal Matrix Composites

By

İsmail TİRTOM

**A Dissertation Submitted to the
Graduate School in Partial Fulfillment of the
Requirements for the Degree of**

MASTER OF SCIENCE

**Department: Material Science and Engineering
Major: Material Science and Engineering**

**Izmir Institute of Technology
Izmir, Turkey**

September, 2002

ACKNOWLEDGEMENTS

It is a pleasure for the author to express his sincere gratitude to his supervisor, Assoc. Prof. Dr. Mustafa GÜDEN for his invaluable guidance, continual supports and constant encouragement throughout the course of this study.

The author is grateful to Assist. Prof. Dr. Hasan YILDIZ and Assist. Prof. Dr. Gamze TANOĞLU for their suggestions and comments.

Finally, the author wishes to express his thanks to his family for their help and support during his studies.

ABSTRACT

A numerical investigation has been conducted on the strain rate dependent compression mechanical behavior of a SiC-particulate reinforced Al (2024-O) metal matrix composite. The effect of particle volume fraction on the strain rate sensitivity of the composite was determined using axisymmetric Finite Element unit cell models, where the particles are treated as elastic spheres embedded within a visco-plastic matrix, implemented in LUSAS Finite Element Analysis program. Particles are taken to be elastic, equal-sized, spherical and uniformly distributed in the matrix. The strain rate dependent constitutive behavior of the matrix material uses a linear relation between stress and strain rate formulation and is obtained from independent experimental results on the matrix. The flow stress of the composites is predicted over a range of strain rates for different particle volume fractions. Numerical results of the flow stress and strain rate sensitivity of the composite were also compared with those of experimental results, for 15% SiC particle reinforced 2024-O Al metal matrix composite. Influence of particle shape on the behavior of the MMC at high strain rates is also investigated. A unit cell, which is an elastic cylinder embedded within a visco-plastic matrix, is used. It is also shown that the rate dependent flow stress and local stress in the microstructure are influenced by particle shape. If reinforcement edge sharpness increases, local stress increases at that area. The results show that both the flow stress and the strain rate sensitivity increase with increasing volume fraction of the reinforcement due to the constraining effect of the reinforcement. Numerical calculations have shown an increased strain rate sensitivity of the composite over the matrix alloy. The discrepancy found between numerical and experimental results was finally discussed based on geometrical and microstructural parameters that might affect the composite flow stress and strain rate sensitivity.

ÖZ

SiC-partikül takviyeli Al (2024-O) metal matrisli kompozit malzemenin, deformasyon hızına duyarlı basma davranışı nümerik olarak incelenmiştir. Parikül hacim oranının, kompozit malzemenin deformasyon hızı duyarlılığına etkisi, LUSAS Sonlu Elemanlar programında oluşturulan bir eksenel-simetrik sonlu elemanlar birim hücre modeli ile belirlenmiştir. Birim hücrede küresel partikülün elastik ve matrisin visko-plastik davranış gösterdiği kabul edilmiştir. Ayrıca partiküller eşit boyutlu ve matris içinde homojen dağıldığı varsayılmıştır. Matrisin deformasyon hızına duyarlı davranışı, deneysel gerilme-deformasyon hızı verilerinden elde edilen lineer bir ilişki ile formule edilmiştir. Kompozitin farklı deformasyon hızlarındaki ve farklı partikül hacim oranlarındaki gerilme-birim şekil değişim grafikleri nümerik olarak elde edilmiştir. Nümerik olarak hesaplanan gerilme ile deformasyon hızı duyarlılığı sonuçlarından % 15 SiC partikül takviyeli Al metal matrisli kompozit için elde edilenleri deneysel sonuçlar ile karşılaştırılmıştır. Nümerik hesaplamalar, kompozitin deformasyın hızı duyarlılığının matris malzemesinden yüksek olduğunu göstermiştir. Kompozitin deformasyon hızı duyarlılığının artan partikül hacim oranı ile de arttığı hesaplanmıştır. Ayrıca kuvvetlendiricinin şeklinin kompozitin davranışına etkiside incelenmiştir. Bu inceleme için birim hücrenin içine silindirik bir kuvvetlendirici yerleştirilmiştir. Sonuç olarak kompozitin deformasyon hızına duyarlı basma davranışının ve birim hücre içinde oluşan bölgesel gerilmelerin kuvvetlendiricinin şeklinden etkilendiği görülmüştür. Nümerik ve deneysel sonuçlar arasında gözlenen farklılıklar, kompozitin deformasyon duyarlılığı ve gerilme-birim deformasyon davranışını etkileyebilecek geometrik ve mikroyapısal parametrelerle tartışılmıştır.

TABLE OF CONTENTS

LIST OF FIGURES

LIST OF TABLES

CHAPTER 1

INTRODUCTION

Metal Matrix Composites (MMCs) exhibit a significant improvement in mechanical performance over monolithic alloys in many structural applications. Some specific advantages include high specific modulus and strength, high strength/weight ratio and high corrosion and temperature resistance [1]. Applications in which the dynamic response of MMCs is important include aerospace and automobile components exposed to crashing and metal forming processes.

The quasi-static mechanical properties and failure mechanisms of particle, whisker and long and short fiber reinforced MMCs have been well characterized [2-6]. Theoretical and numerical investigations have been performed to predict the stiffness and the strength of the composites, given the mechanical properties of the matrix and reinforcement phases [7-10]. The effects of reinforcement volume fraction, size, shape, aspect ratio and particle distribution on the plastic deformations and failure mechanisms under quasi-static loading have been extensively studied [7,10-12].

The mechanical properties under high strain rates are not well investigated and developed as much. Much of the high strain rate studies on these materials have been reviewed in references 7,22. The first experimental investigation of high strain rate behavior of MMCs is due to Harding *et al*. [13] and Marchand *et al.* [14]. Studies of the high strain rate behavior of specific MMCs include those of Perng *et al*. [15], Hong and Gray [16], Mukai et al. [17], Yadav et al. [18], Chichili and Ramesh [19], Vaidya *et al.* [20], Gray et al. [21] and Guden and Hall [22]. A higher strain rate sensitivity of the composite compared with matrix material is commonly found in these studies. Yadav et al. [23] numerically indicated that the effect of strain rate in particle reinforced MMCs would be strongly dependent on the particle volume fraction. Bao and Lin [10] and Yadav [23], based on axisymmetric unit cell model, showed that the effect of strain rate is coupled with the particle volume fraction and the strain rate hardening of the composite may be significantly higher than that of the matrix due to the constraining effect of particles. Li and Ramesh [7] also studied the effects of particle shape and aspect ratio on the high strain rate response of SiC-particle (SiC_p) reinforced MMCs,

and concluded that both variables have a strong influence on the flow stress at high strain rates.

High strain rate mechanical properties are a great concern of the design engineers as the mechanical properties of materials are significantly affected by the loading rates. Many materials, for example, show more brittle but stronger mechanical response to the increasing loading rates. High strain rate material properties are important in impact-related applications such as collisions of automobiles, hitting of external objects to the structural elements (e.g. aeroplane wings, satellite), impinging of projectiles to armors and so on. In modeling these structures, high strain rate mechanical properties are certainly required in order to increase their confidence limits. Many of the high strain rate testing methods however necessitate the utilization of expensive instrumentation and time-consuming specimen preparation and data analysis involving complex wave propagation. Models that could predict the rate dependent material properties with limited number of tests are therefore very attractive for the design engineers.

This study presents a systematic computational investigation of the compression stress-strain curves of a SiC_p reinforced Aluminum (Al) MMC, with different particle volume fractions, over a wide range of strain rate from quasi-static ($10^{-3}s^{-1}$) to high strain rates ($\sim 10^4\ s^{-1}$). Axisymmetric unit cell models with varying boundary conditions were implemented in LUSAS Finite Element Model (FEM) program. Rigid ceramic particle embedded into viscoplastic matrix was assumed to have strain rate insensitive elastic modulus in the studied strain rate regime. The strain rate dependent matrix flow properties were therefore considered to be the only factor affecting composite strain rate dependent mechanical properties. The matrix flow stress behavior (constitutive equation) was determined through limited number of tests conducted at quasi-static and high strain rates. The numerical results of the models were compared with the experimental results in order to validate the model capability to predict the stress-strain curves of the similar composites at different strain rates.

CHAPTER 2

METAL MATRIX COMPOSITES

Metal Matrix Composites (MMCs) refer to a composite material group of reinforced metallic matrices. The reinforcement is usually a ceramic based material in one of the forms; particle, whisker and/or short and long fibers. The reinforcement enhances the strength and thermomechanical properties while the ductile metallic matrix confers toughness and strength on the composite. The function of the matrix in MMCs is different from that in polymeric matrix composites in which the matrix contribution to the strength of the composite is insignificant. Strengthening of the matrix itself can, however, contribute to the strength of the MMC and can be easily achieved using conventional strengthening methods developed for metallic materials such as alloying element additions and precipitation or dispersion hardening.

2.1. History

Initial studies on MMCs started in the 1960s for the needs of the aerospace industry. The first MMC produced was 60% boron monofilament reinforced Al-based composite and used in the U.S. Space Shuttle as tubing for cargo bay stiffeners [25]. The manufacturing process for production of monofilament component preforms was quite expensive and consisted of a variety of complex processes such as bonding of lay-up of filaments to Al-alloy foils and consolidation by diffusion bonding [26]. Manufacturing which involves relatively cheaper and simpler processes such as casting and powder metallurgy (P/M) techniques incorporating particle, whisker and short fiber reinforcements was started to be successfully applied to MMCs in 1980s.

The first commercial application of MMCs in the automotive industry was achieved in 1983 when Toyota replaced a diesel piston with a Saffil™ Short Fiber (SF)-reinforced Al MMC. Later, Honda replaced the engine block on one of its models with a hybrid (Saffil and carbon SF) Al-Si MMC lined Al-block. The application areas of MMCs have widened to several different industries including automotive, aerospace and sports industries. The potential applications of MMCs in the aerospace industry have been considered by Ponzi [27].

2.2. Matrix

The following criteria may be considered to be important for the selection of the matrix: The chemical compatibility of the alloy with reinforcement, ability of the alloy to wet reinforcement, properties of the alloy and processing behavior. The choice of matrix alloy is usually between the light metals, Al, Mg and Ti, and their alloy groups diverse in physical and mechanical properties.

Relatively good load transfer to the reinforcing phase is ensured by a strong interface between matrix and reinforcement. That is provided with adequate wetting of matrix to reinforcement. This frequently, however, involves chemical reactions between fiber and matrix, which in turn degrade the fiber properties. A compromise, therefore, it is needed to provide strong bonding without leading to excessive fiber degradation by chemical reactions. Nearly all commercial fibers are poorly wetted by Al and its alloys. Al can also easily react with C and SiC reinforcements. Several methods are proposed and applied to increase wettability such as addition of alloying elements, modification of the oxide layer on the metal surface, use of coatings and pre-treatment of the reinforcement [26].

2.3. Reinforcement

The most widely used reinforcements include SiC whisker, particle and long fiber and Al_2O_3 particle, short and long fibers. The composite microstructures may be grouped as continuous fiber, short fiber and particle reinforced MMCs (Figure 2.1 a, b and c). Further distinctions may be drawn on the basis of fiber diameter and orientation distribution.

Reinforcement type, size and geometry can easily be varied, depending on the desired mechanical properties of the MMC. Particle reinforced MMCs have almost isotropic mechanical properties. With whisker, short and long fibers reinforcement, directional strengthening can be achieved depending on fiber distribution and orientation. A list of selected whisker and particle reinforcements used in MMCs is tabulated in Tables 2.1 together with mechanical and physical properties.

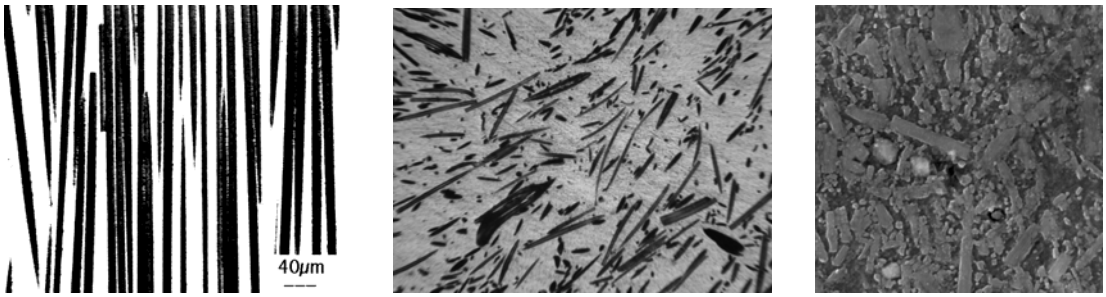

(a) **(b)** **(c)**

Figure 2. 1. (a) FP Alumina long fiber **(b)** alumina saffil short fiber and **(c)** SiC whisker reinforced Al MMCs [1].

Table 2.1. Mechanical and physical properties of particulates and whiskers [1].

Whisker or particle	Tensile Strength (GPa)	Elastic Modulus (GPa)	Density (kgm^{-3})	Diameter (μm)	CTE ($10^{-6}K^{-1}$)
Al_2O_3		430	3.8	1-50	7
B_4C	2.1	480	2.5	1-50	
SiC	3.2	450	3.2	1-50	4
TiC		230	4.9		
SiC_w	3.1,<21	450, <700	3.2	0.1-1	4
Si_3N_{4w}	2-4, <14	350-385	3.1		

2.4. Manufacturing

Liquid/preform infiltration (squeeze infiltration), slurry casting, spray casting and P/M routes are the processes successfully applied to MMCs. Squeeze casting is the most widely used technique for MMC manufacturing in which the liquid metal is infiltrated through a preheated preform and the melt solidifies under pressure. Squeeze casting is suitable for all types of fiber reinforced MMCs. In slurry casting, also called compo-casting, the particles are added to the semi-solid slurry and the slurry is then agitated mechanically to promote reinforcement wetting with liquid and to avoid reinforcement agglomeration and sedimentation. Slurry casting can be applied to short fiber, whiskers and particulates forms of the reinforcements but is mostly used for manufacturing of particulate reinforced MMCs [1]. In spray casting, the droplets of the molten metal are sprayed together with reinforcement phase and collected on a substrate. The process is applicable for particulate and continuous fiber reinforcements. In the P/M route, the reinforcement and metal powders are blended and the blend is then consolidated at high temperature and pressure. The process is usually followed by commercial metal forming

techniques such as extrusion and rolling. The P/M route is applicable to short fiber, whisker and particulate reinforced MMCs.

2.5. Basic Mechanics

There are several methods to predict MMCs mechanical properties. These include the slab, the shear-lag, Eshelby and FE models. The first two methods will be summarized shortly in this section and detailed information on Eshelby method is for example found in [1]. FEM will be explained separately in Chapter 3.

The slab model treats the composite as if it were composed of two slabs bonded together; one of which is matrix and the other is the reinforcement as shown in Figure 2.2 for a transversely loaded long fiber composite. The load sharing between fiber and matrix is then used to calculate composite strength in fiber and normal to fiber directions.

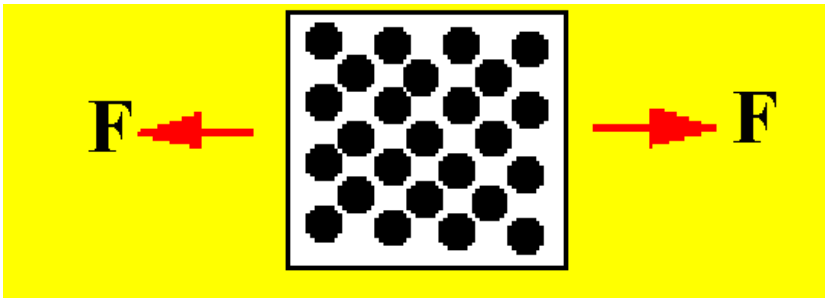

(a)

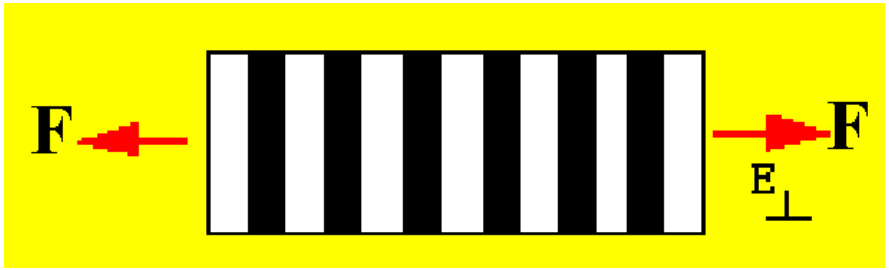

(b)

Figure 2. 2. (a) Long fiber composite loaded normal to the fiber plane and **(b)** slab model presentation [1].

Based on this model, following equations are derived for the tensile strength of the unidirectional long (Eq. 2.2) and short fiber (Eq. 2.3) composites in the fiber direction:

$$\sigma_c = V_f\sigma_f + (1 - V_f)\,\sigma_m^* \tag{2.1}$$

$$\sigma_c = V_f\sigma_f\left(1 - \frac{l_c}{2l_f}\right) + (1 - V_f)\,\sigma_m^* \quad l_c \le l_f \tag{2.2}$$

$$\sigma_c = \tau_m V_f\left(\frac{l_f}{d_f}\right) + (1 - V_f)\,\sigma_{um} \quad l_c > l_f \tag{2.3}$$

where σ_c is the composite strength, σ_f is the fiber strength, l_f is the fiber length, σ_m^* is the matrix stress at fiber failure strain, τ_m is the interfacial stress, σ_{um} is the matrix tensile strength, V_f is the volume fraction and l_c is the critical fiber length and given by

$$l_c = \frac{\sigma_f d_f}{2\tau_m} \tag{2.4}$$

In many cases the interface strength is assumed to be the yield strength of the matrix in shear and therefore can be considered as $\sigma_{my}/2$. Equation 2.1 is used for continuous fiber reinforced composites and Equations 2.2 and 2.3 are for the longitudinal strength of short fiber reinforced composites when taking the fiber length effect into account.

One of the most widely used models describing loading of an aligned short fiber composite is the shear-lag model, originally proposed by Cox [28]. The shear-lag model formulates fiber and matrix shear stresses via load transfer from matrix to interface. It is therefore suitable for short fibers aligned to loading axis (Figure 2.3). For elastic deformation, composite strength is given by the following equation:

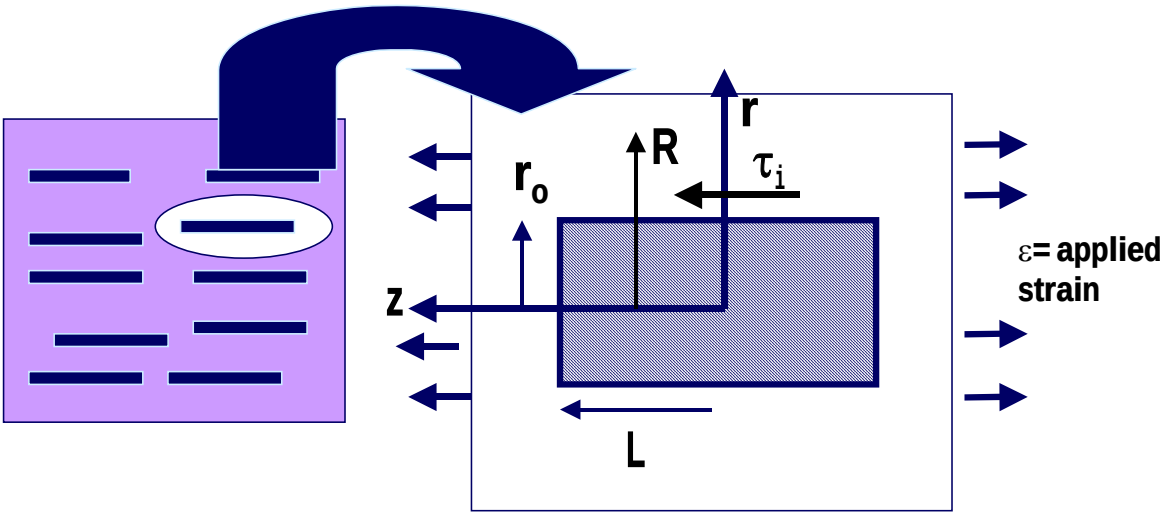

Figure 2.3. Schematic of the shear-lag model; τ_i : interface shear stress r_0 : fiber radius, R: point where matrix has uniform strain [1].

$$\sigma_c = fE_f\varepsilon\left[1-\frac{\tanh(ns)}{ns}\right]+(1-f)E_m\varepsilon \tag{2.5}$$

where E_f and E_m are the modulus of fiber and matrix respectively, s is the fiber aspect ratio (fiber length/diameter) and n is

$$n^2=\frac{2E_m}{E_f(1+\nu_m)\ln(1/f)} \tag{2.6}$$

where ν_m is the matrix Poissons ratio.

The continuum approach to predicting the modulus and strength of composites containing long fibers can be successfully applied. The role of the matrix is to transfer load to the strong fibers and the composite attains its ultimate strength when the fibers fracture. In the case of discontinuous fiber reinforced composites containing fibers whose length is less than the critical length, the ultimate stress is reached when the fibers debond and are pulled out of the matrix. However, the continuum models are argued to give rough estimations of strength in the particulate and whisker reinforced composites by ignoring the effects of particle size and unrelaxed stresses in the

composite. The micromechanical approach is believed to give better estimates of the flow stress of discontinuously reinforced MMCs by taking into account the dislocation mechanism in the matrix.

The micromechanical approach considers several possible barriers to dislocation motion including factors such as internal stress, residual dislocations, particles, grain boundaries and substructure. The difference in coefficient of thermal expansion (CTE) between matrix and fiber almost unavoidably results in internal stresses as the composite cools down from the elevated production temperature. Part of these stresses is relieved by generation of dislocations and the remaining misfit gives rise to a build-up of tensile residual stresses in the matrix.

The strengthening due to small particles can be estimated using the Orowan equation for bowing dislocations around particles giving dislocation loops around them

$$\sigma = \frac{2Gb}{\chi} \tag{2.7}$$

where χ is the distance between particles. The Orowan strengthening in MMCs is argued to be small due to the relatively large particle size and the distance between particles. The Orowan strengthening is calculated to be ~6 MPa in a composite containing 3 μm particles with $17V_f$%. However, it may be significant in the age hardenable matrices where residual dislocations may affect the precipitate nucleation rate and size. The MMCs usually have finer grain size as compared to monolithic alloys. The typical grain sizes in particulate and whisker reinforced MMCs are around 10 μm. The strengthening due to grain size refinement in composite can be determined using the Hall-Petch equation

$$\Delta\sigma_G = k_y d_g^{-\frac{1}{2}} \tag{2.8}$$

where k_y is a constant and d_g is the grain size. The grain size refinement is calculated to be significant in MMCs containing grain sizes in the order of 1-10 μm. The contribution from subgrains near to the reinforcement can be also predicted using the Hall-Petch Equation.

CHAPTER 3

FINITE ELEMENT MODEL

3.1. The Finite Element Method

The Finite Element Method is a numerical method for solving problems of engineering and mathematical physics. It is useful for problems with complicated geometries, loadings, and material properties where analytical solutions are difficult to obtain or can not be obtained [28]. Until the advent of computers, the only way to test a designed structure was to build a prototype and carry out the necessary tests. Today computers allow designs to be assessed much more quickly and easily.

In order to calculate the response of a complex shape, that we called engineering problem, to any external load the complex shape must be divided into smaller and simple shapes as shown Fig. 3.1. These are the finite elements that give the method its name. The shape of each finite element is defined by the coordinates of its nodes. Adjoining elements with common nodes will interact each other.

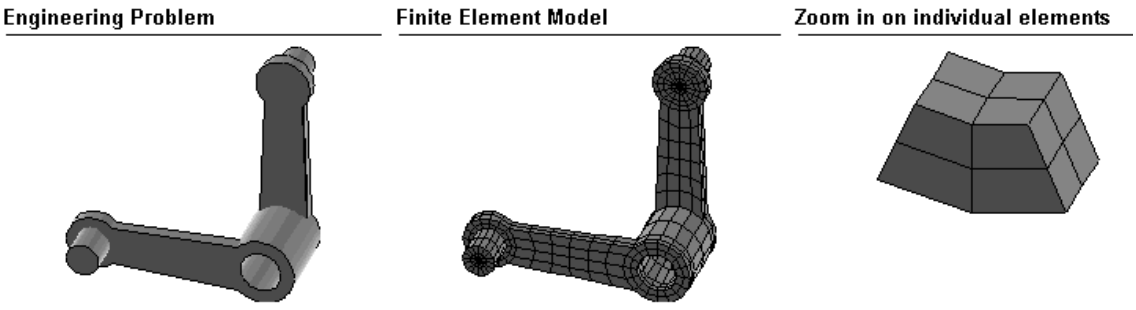

Figure 3.1. (a) A complex engineering structure **(b)** its FEM and **(c)** elements [29].

The real engineering problem responds in an infinite number of ways to external forces. The manner in which the Finite Element Model will react is given by the degrees of freedom, which are expressed at the nodes. For example, a three-dimensional solid element has three degrees of freedom at each node representing the three global directions in which it may move. If one can express the response of a single Finite Element to a known stimulus, a model for the whole structure can be build up by

assembling all of the simple expressions into a set of simultaneous equations with the degrees of freedom at each node as the unknowns. These are then solved using a matrix solution technique. For a mechanical analysis, once the displacements are known, the strains and stresses can be calculated. For a thermal analysis, the gradients and fluxes can be calculated from the potentials [29].

3.2. Static Analysis

Static analysis is one of the most commonly used analysis of engineering structures. As its name implies, in this analysis, loads are applied instantaneously; that is, any transient effect is ignored. For linear static analysis the loaded body instantaneously develops a state of internal stress so as to equilibrate the total applied loads. The overall structural response, both the geometric and material response, is considered to be linear in linear static analysis. This is often represented by the extension of a spring with a stiffness constant of k (Figure 3.2).

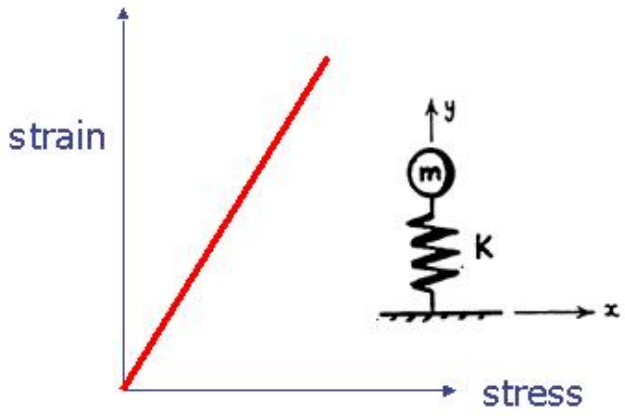

Figure 3.2. Linear elastic stress-strain behavior of a spring.

Consider the equilibrium of a general three-dimensional body subject to surface (t), body (b) and concentrated (F) forces. The body will be displaced from its original configuration by an amount **u**, which gives rise to strain **ε** and corresponding stress **σ**. The governing equations of equilibrium may be derived by utilizing the principle of virtual work. This states that, for any small virtual displacements δu imposed on the body, the total internal work must equal the total external work for equilibrium to be maintained, i.e.

$$\int_v \delta\varepsilon^T \sigma \, dv = \int_v \delta u^T f \, dv + \int_s \delta u^T t \, ds + \sum du^T F \tag{3.1}$$

where $\delta\varepsilon$ are the virtual strains corresponding to the virtual displacements δv.

In finite element analysis, the body is approximated as an assemblage of discrete elements inter-connected at nodal points. The displacements within any element are then interpolated from the displacements at the nodal points corresponding to that element, i.e. for element e

$$u^{(e)} = N^{(e)} a^{(e)} \tag{3.2}$$

where $N^{(e)}$ is the displacement interpolation or shape function matrix and $a^{(e)}$ is the vector of nodal displacements. The strains $\varepsilon^{(e)}$ within an element may be related to the displacements $a^{(e)}$ by

$$\varepsilon^{(e)} = B^{(e)} a^{(e)} \tag{3.3}$$

where B is the strain-displacement matrix. For linear elasticity, the stresses σ within the finite element are related to the strains using a constitutive relationship of the form

$$\sigma^{(e)} = D^{(e)} (\varepsilon^{(e)} - \varepsilon_0^{(e)}) + \sigma_0^{(e)} \tag{3.4}$$

where $D^{(e)}$ is a matrix of elastic constants, and $\varepsilon_0^{(e)}$ and $\sigma_0^{(e)}$ are the initial stresses and strains respectively.

Using (3.2), (3.3) and (3.4), the virtual work equation (3.1) may be discretised to give

$$\sum_{e=1}^{n} \delta a^T \int_v B^{(e)T} D^{(e)} B^{(e)} dV a =$$

$$\delta a^T \left[\sum_{e=1}^{n} \int_v N^{(e)T} f^{(e)} dV + \sum_{e=1}^{n} \int_s N_s^{(e)} - \sum_{e=1}^{n} \int_v B^{(e)T} (\sigma_0^{(e)} - D^{(e)} \varepsilon_0^{(e)}) dV + F \right] \quad (3.5)$$

where $N_s^{(e)}$ are the interpolation functions for the surfaces of the elements and n is the number of elements in the assemblage.

By using the virtual displacement theorem, the equilibrium equations of the element assemblage becomes

$$Ka = R \quad (3.6)$$

where K is the structure stiffness matrix, defined as

$$K = \sum_{e=1}^{n} \int_v B^{(e)T} D^{(e)} B^{(e)} dV \quad (3.7)$$

and R is the structure force vector, defined as

$$R = R_b + R_s - R_o + R_e \quad (3.8)$$

where R_b is the force vector due to the element body loads,

$$R_b = \sum_{e=1}^{n} \int_v N^{(e)T} f^{(e)} dV \quad (3.9)$$

R_s is the force vector due to the element surface tractions,

$$R_s = \sum_{e=1}^{n} \int_s N_s^{(e)T} t^{(e)} dV \quad (3.10)$$

R_0 is the force vector due to the initial stresses and strains,

$$R_0 = \sum_{e=1}^{n} \int_v B^{(e)T} (\sigma_0^{(e)} - D^{(e)} \varepsilon_0^{(e)}) dV \tag{3.11}$$

and R_c is the force vector due to concentrated loads,

$$R_0 = F \tag{3.12}$$

Equation (3.6) may be utilized for situations where the applied loading is independent of time or when the load level changes very slowly. If rapid changes in the load level occur, inertia and damping forces must be included in the equilibrium equations.

3.3. Plasticity and Non-Linear Analysis

3.3.1. Basics of Plasticity and Related Material Properties

When a material deforms above a critical stress or strain, deformation becomes permanent; that is the material cannot recover its original shape. Plastic deformation is therefore irreversible, although there always exists small anelastic strain which is usually ignored in continuum mechanics. Contrary to elastic deformation, the stress-strain relation is usually non-linear in plastic deformation. Many plasticity-related properties however can be easily extracted from the uniaxial stress-strain curve.

3.3.1.1. Proportional Limit and Yield Point

The point at which the stress-strain curve deviates from linearity is called the *proportional limit* (Figure 3.3). On a stress-strain curve, a tangent line drawn in the elastic region will give the proportional limit. The yield point is determined by a repeated loading and unloading and simultaneously recording the strain until the point reached where strain does not return back to zero. The load at which the irreversible point is reached is called the yield point (Figure 3.3). Since the yield point determination is difficult to perform and there is usually little difference between the yield point and the proportional limit, in many FE analysis programs they are generally assumed to be the same.

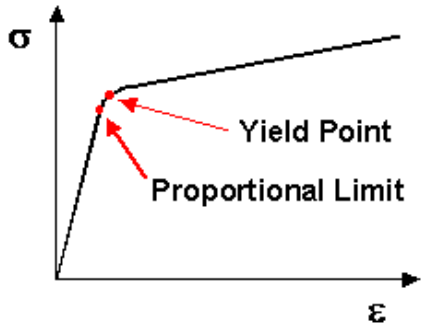

Figure 3.3. Proportional and yield point on a stress-strain curve [43].

3.3.1.2. Strain Hardening

The increase of the yield stress with increasing strain is called *strain hardening.* Strain hardening behavior is usually characterized as being either *elastic perfectly plastic* or *strain hardening*. In the former, the yield stress remains constant above the yield strain (Figure 3.4(a)) and in the latter stress increases with strain either linearly (Figure 3.4(b)) or non-linearly.

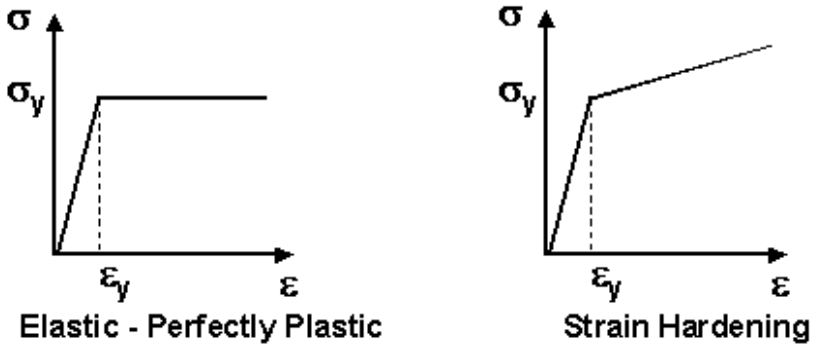

(a) **(b)**

Figure 3.4. Uniaxial stress-strain curves; (a) elastic-perfectly plastic and (b) strain hardening material [43].

Incremental plasticity theory provides a mathematical relationship that characterizes the increments of stress and strain (Dσ and De) to represent the material behavior in the plastic range. There are three basic components of the incremental plasticity theory: yield criterion and flow and hardening rules.

3.3.1.3. Yield Criterion

In uniaxial tensile test, the yield stress or proportional limit is determined based on the measured stress-strain data. However, for a multiaxial state of stress, it is necessary to define a yield criterion. The *yield criterion* is a single-valued (scalar) measure of the stress state that may be readily compared to the yield stress from the uniaxial test. A common yield criterion is the von Mises yield criterion. It states that yielding begins whenever the internal energy of distortion (equivalent stress) exceeds a certain value. The von Mises equivalent stress is defined as:

$$\sigma_e = \sqrt{\frac{1}{2}[(\sigma_1 - \sigma_2)^2 + (\sigma_2 - \sigma_3)^2 + (\sigma_3 - \sigma_1)^2]} \tag{3.13}$$

where σ_1 , σ_2 and σ_3 are the principal stresses. Yielding occurs when the equivalent stress exceeds the yield stress of the material:

$$\sigma_e > \sigma_y \tag{3.14}$$

In principal stress space the von Mises yield criterion is represented by a cylindrical *yield surface* aligned along the axis $\sigma_1 = \sigma_2 = \sigma_3$ in 3D (Figure 3.5 (a)) and by an ellipse in 2D (Figure 3.5 (b)). Any stress state outside the yield surface causes yielding.

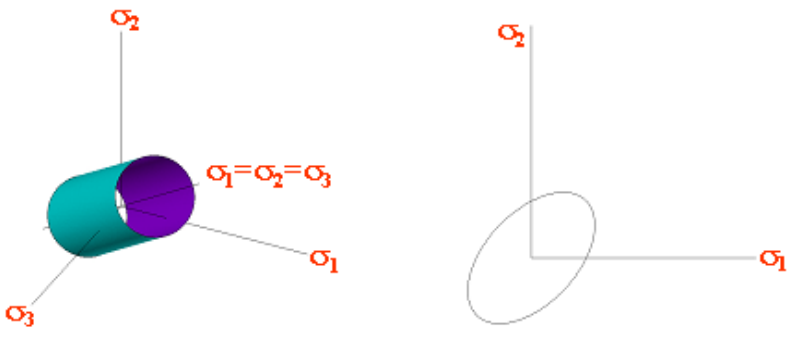

(a) **(b)**

Figure 3.5. Representation of the von Misses yield surface in **(a)** 3D and **(b)** 2D [43].

.

3.3.1.4. Flow Rule

The *flow rule* prescribes the direction of the plastic straining when yielding occurs. It defines how the individual plastic strain components (e_x^{pl}, e_y^{pl}, etc.) develop with yielding. Flow equations, which are derived from the yield criterion, typically imply that the plastic strains develop in a direction *normal* to the yield surface. Such a flow rule is termed *associative*. If some other flow rule is used (derived from a different function), it is called *non-associative*

3.3.1.5. Hardening Rule

The *hardening rule* describes how the initial yield criterion changes with progressive plastic straining. There are two basic hardening rules used in FEM to prescribe the modification of the yield surface: isotropic and kinematic hardening.

In isotropic hardening the yield surface expands uniformly in all directions with plastic flow (Figure 3.6). The stress-strain behavior for a uniaxial specimen with isotropic hardening is given in Figure 3.7 and it is noted that the subsequent yield in compression is equal to the highest stress attained during the tensile loading. Isotropic hardening is often used for large strain or proportional (non-cyclic) loading simulations.

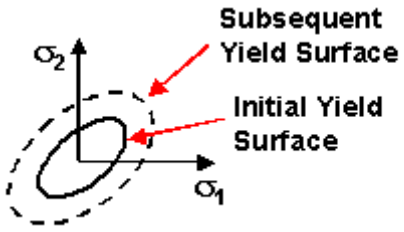

Figure 3.6. Isotropic hardening.

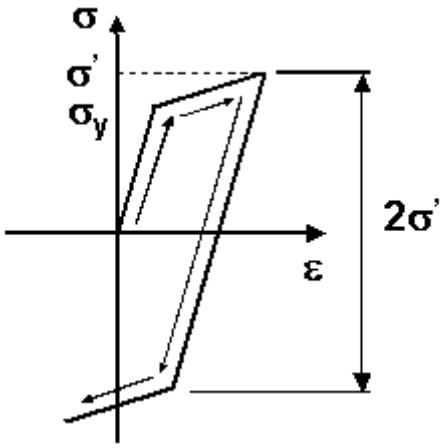

Figure 3.7. Uniaxial stress-strain behavior of a material with isotropic hardening.

In kinematic hardening, the yield surface remains constant in size and translates in the direction of yielding (Figure 3.8). Most metals exhibit kinematic hardening behavior for small strain cyclic loading. The stress-strain behavior for a uniaxial specimen with kinematic hardening is given in Figure 3.9. Note that the subsequent yield in compression is decreased by the amount that the yield stress in tension increased, so that a $2\sigma_Y$ difference between the yields is always maintained. (This is known as the *Bauschinger effect.*). An initially isotropic material is no longer isotropic after it yields and experiences kinematic hardening. For very large strain simulations, the kinematic hardening model can become inappropriate.

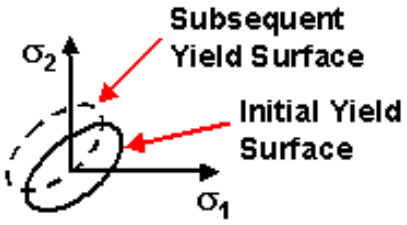

Figure 3.8. Kinematic hardening.

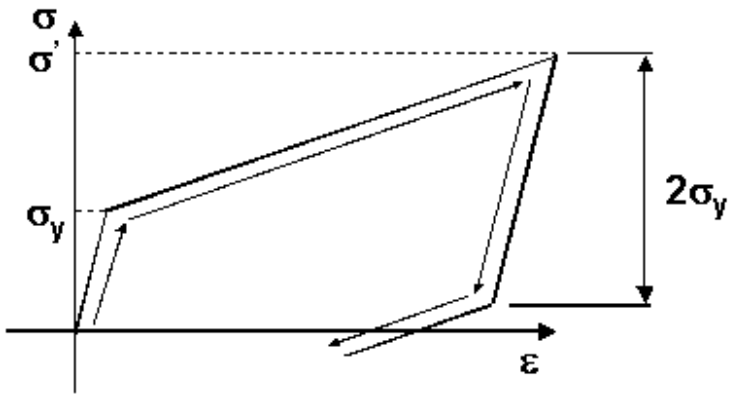

Figure 3.9. Uniaxial stress-strain behavior of a material of kinematic hardening.

3.3.2. Non-linear Analysis

Linear Finite Element Analysis assumes that all materials are linear elastic in behavior and that deformations are small enough to not significantly affect the overall behavior of the structure. This description applies to very few situations but with a few restrictions and assumptions, linear analysis will suffice for the majority of engineering applications. Significant classes of structures do not however have a linear relationship between force and displacement. Since a plot of force versus displacement for such

structures is not a straight line, such structures are said to be non-linear. The stiffness is no longer a constant, K; it becomes a function of applied load, $\mathbf{K^T}$ (the tangent stiffness) (Figure 3.10).

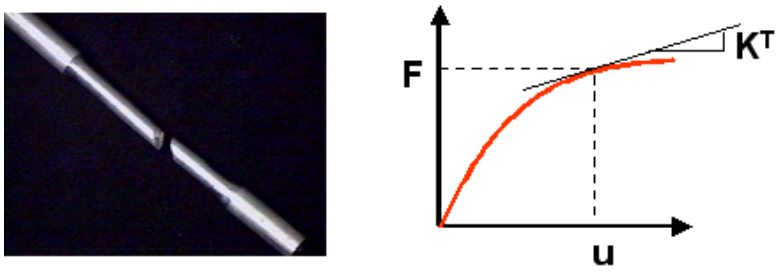

Figure 3.10. A ductile metal tensile test specimen and its non-linear force-displacement behavior [43].

Non-linear structural behavior arises for a number of reasons, which can be reduced to three main categories: (i) Geometric Nonlinearities (large strains, large deflections, stress stiffening), (ii) Material Nonlinearities (plasticity, hyperelasticity, creep) and (iii) Changing Status Nonlinearities (contact, element birth and death), see Figure 3.11.

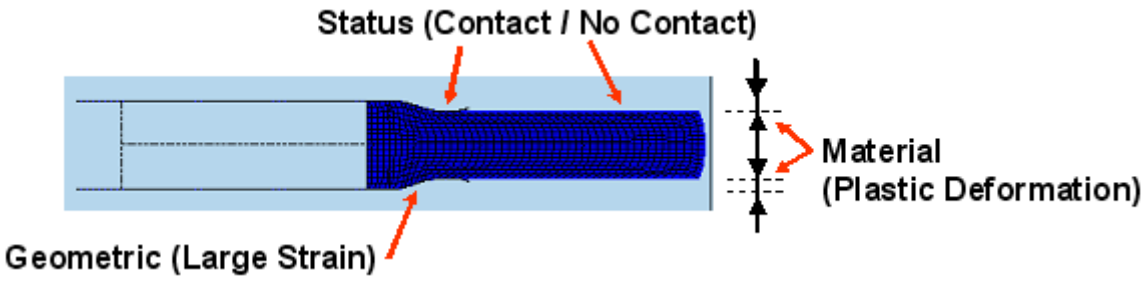

Figure 3.11. Types of nonlinearities in aluminum extrusion process [43].

Materially non-linear effects arise from a non-linear constitutive model (that is, progressively disproportionate stresses and strains). Common examples of non-linear material behavior are the plastic yielding of metals, the ductile fracture of granular composites such as concrete, or time-dependent behavior such as creep.

A non-linear stress-strain relationship is a common cause of non-linear structural behavior as shown in Figure 3.12 in plastically deforming steel and elastically deforming rubber specimens.

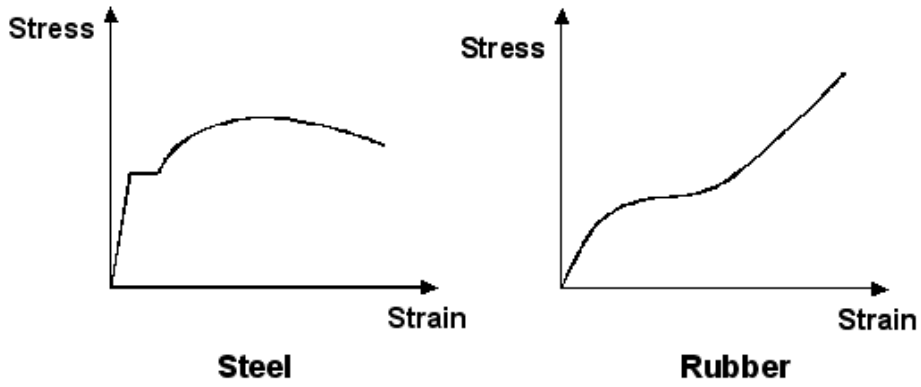

Figure 3.12. Non-linear stress-strain behavior of steel and rubber.

3.4. Non-linear Solution Procedures

For non-linear analysis, since it is no longer possible to directly obtain a stress distribution, which equilibrates a given set of external loads, a solution procedure is usually adopted in which the total required load is applied in a number of increments. Within each increment a linear prediction of the non-linear response is made, and subsequent iterative corrections are performed in order to restore equilibrium by the elimination of the residual or 'out of balance' forces [16].

The iterative corrections are referred to some form of convergence criteria which indicates to what extent an equilibrate state has been achieved. Such a solution procedure is therefore commonly referred to as an incremental-iterative (or predictor-corrector) method shown in Figure 3.13.

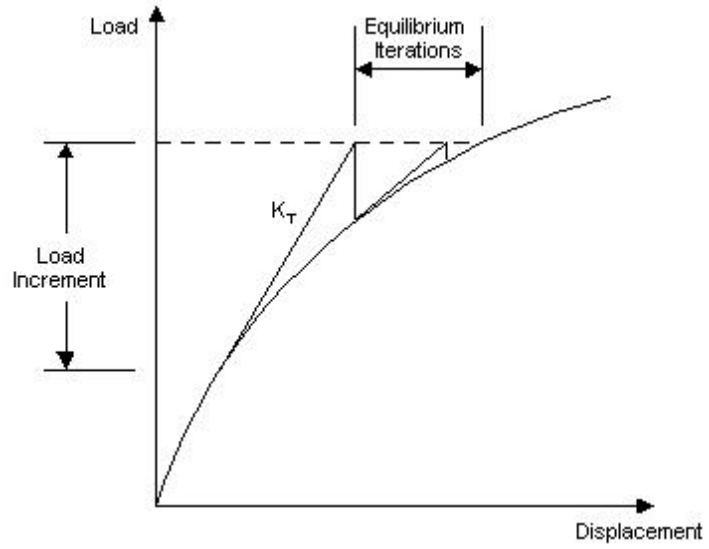

Figure 3.13. Incremental-iterative solution procedure [30].

For the analysis of non-linear problems, the solution procedure adopted may be of significance to the results obtained. In order to reduce this dependence, wherever possible, non-linear control properties incorporate a series of generally applicable default settings, and automatically activated facilities.

3.4.1. Iterative Procedures

In LUSAS, which was used in this study as a numerical tool, the incremental-iterative solution is based on Newton-Raphson iterations. In the Newton-Raphson procedure, an initial prediction of the incremental solution is based on the tangent stiffness from which incremental displacements, and their iterative corrections may be derived.

3.4.1.1. Standard Newton-Raphson procedure

In the standard Newton-Raphson procedure, each iterative calculation is always based upon the current tangent stiffness. For finite element analysis, this involves the formation (and factorization) of the tangent stiffness matrix at the start of each iteration. Although the standard Newton-Raphson method generally converges rapidly, the continual manipulation of the stiffness matrix is often expensive. The need for a robust but inexpensive procedure therefore leads to the development of the family of modified Newton-Raphson methods. The Newton-Raphson method iterates to a solution using the equation:

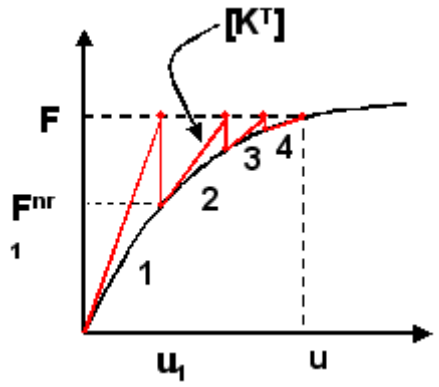

$$[K^T]\{Du\} = \{F\} - \{F^{nr}\} \qquad (3.15)$$

where:

$[K^T]$ = Tangent Stiffness Matrix

$\{Du\}$ = Displacement Increment

$\{F\}$ = External Load Vector

$\{F^{nr}\}$ = Internal Force Vector(sum of element stresses)

Each iteration is a separate pass through the equation solver. One iteration is as expensive as a single linear static analysis. The difference between external and internal loads, $\{F\} - \{F^{nr}\}$, is called the *residual*. It is a measure of the force imbalance in the structure. The goal is to iterate until the residual becomes acceptably small; that is, until the solution *converges*. When convergence is achieved, the solution is in *equilibrium*, within an acceptable tolerance.

3.4.1.2. Newton Iteration

Although Newton-Raphson iteration is stable and converges quadratically (provided the initial estimate is close enough to the solution), it has the disadvantage that the tangent stiffness matrix needs to be inverted during each iteration. Also, it may fail to converge when extreme material nonlinearities are present in a structure. For this case, modified Newton iteration may be more effective. With modified Newton iteration, the current tangent stiffness matrix is replaced with a previous stiffness matrix, say from the beginning of the increment. This reduces the cost of the computation/iteration as the factorization of the tangent stiffness matrix is not required for every iteration. Three common forms of modified Newton-Raphson are initial stiffness method, KT1 method, KT2 method (Figure 3.14(a), (b) and (c)).

The convergence rate of modified Newton iteration is not quadratic and the procedure often diverges. However, when coupled with the line search procedure it forms an iteration algorithm that is particularly suitable for structures exhibiting extreme material nonlinearity. Newton-Raphson iteration, which also was used in this study, is more effective for geometrically non-linear problems than modified Newton iteration.

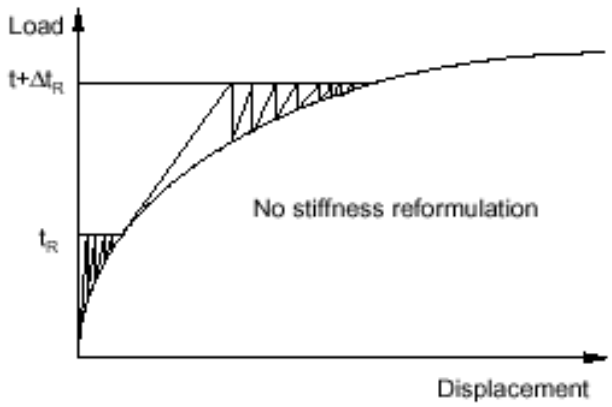

(a) Initial Stiffness Method

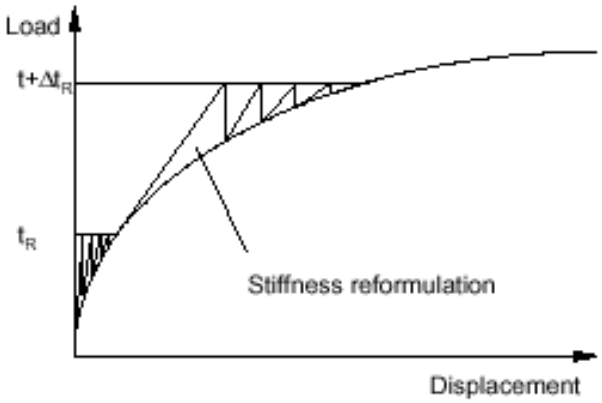

(b) KT1 Method

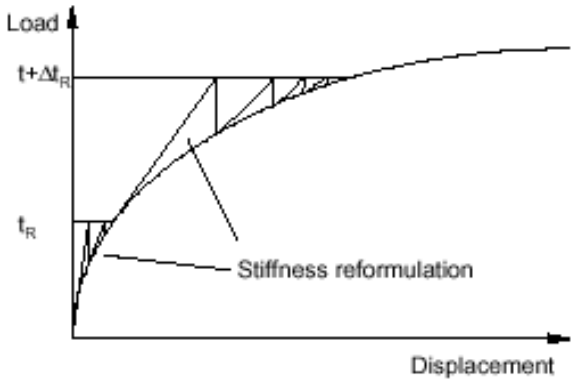

(c) KT2 Method

Figure 3.14. Common forms of modified Newton iteration [30].

3.4.1.3. Iterative Acceleration (Line Searches)

A slow convergence rate may be significantly improved by employing an iterative acceleration technique. In cases of severe and often localized nonlinearity, encountered typically in materially non-linear or contact problems, some form of acceleration may be a prerequisite to convergence.

In LUSAS, iterative acceleration is performed by applying line searches. In essence, the line search procedure involves extra optimization iterations in which the potential energy associated with the residual forces at each iterative step are minimized. Line search application is controlled via parameters on the iteration section of the non-linear control properties. The selection of line search parameters is problem dependent and largely a matter of experience. However, a maximum of 3 to 5 line search iterations

with a tolerance of 0.3 to 0.8 is usually sufficient (the closer the tolerance is to unity, the more slack the minimum energy requirement).

3.4.2. Incremental Loading

Incrementation for non-linear problems may be specified in four ways:

- Manual Incrementation where the loading data in each load increment is specified separately.
- Automatic Incrementation where a specified load case is factored using fixed or variable increments.
- Mixed Incrementation: Mixed manual and automatic incrementation.
- Load Curves where the variation of one or more sets of loading data is specified as a load factor vs. load increment or time step load curve.

The choice and level of incrementation will depend on the problem to be solved.

CHAPTER 4

UNIT CELL AND MODEL MATERIAL

4.1. Unit Cell Model

4.1.1. Geometry

Ceramic particles are assumed spherical, elastic and homogeneously dispersed in the matrix. A particle in a cylindrical matrix phase is taken as the unit cell and used to model the whole composite structure [7,8,10-12] (Figure 4.1). Due to symmetry, only one quarter of the axisymmetric unit cell is used in the model calculations. The geometrical parameters of the model are particle radius, unit cell cylinder radius and height, as depicted in Figure 4.2.

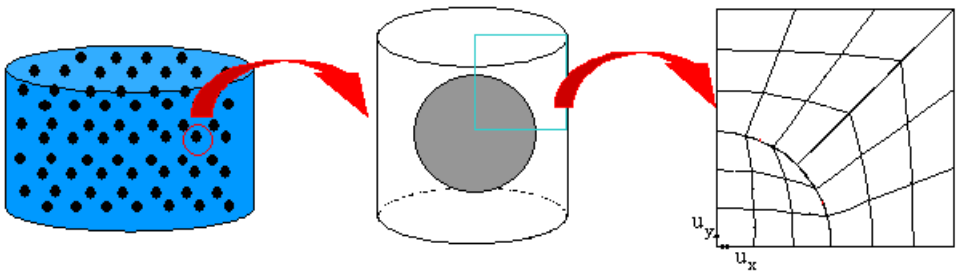

(a) **(b)** **(c)**

Figure 4.1. Schematic of the axisymmetric unit cell model; **a)** composite, **b)** unit cell and **c)** a quarter of the unit cell.

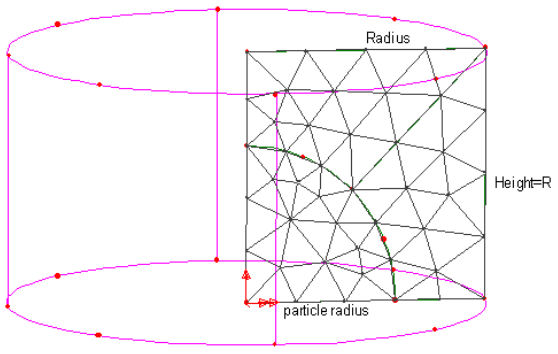

Figure 4.2. Geometrical parameters of the model.

The effect of reinforcement volume fraction on the stress-strain behavior of the SiCp/2024-O Al MMC (the model material) was investigated using four different unit cell models containing 5, 10, 15 and 25 volume percentage of SiC_p as shown sequentially in Figure 4.3(a), (b), (c) and (d). The particles are assumed to be spherical and homogeneously distributed in the composite with an average particle size of 30 μm. The particle packing geometry was chosen as a square. The height or length of the unit cell was calculated using the following equation:

$$R = \left(\frac{4r^3}{6f} \right)^{1/3} \tag{4.1}$$

where f is the particle volume fraction, r is the particle radius and R is the length of the unit cell. Since the particle packing geometry is a square, the height of the cylinder is equal to its diameter.

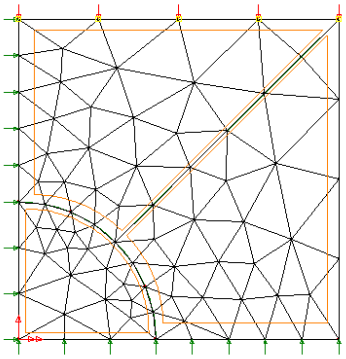

(a)

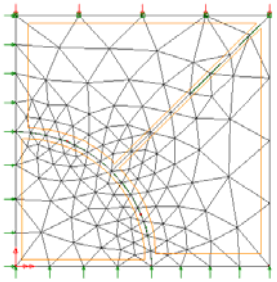

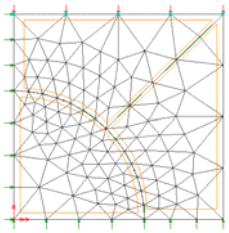

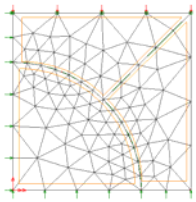

(b) **(c)** **(d)**

Figure 4.3. Unit cell composite models based on; **a)** 5, **b)** 10, **c)**15 and **d)**25% SiC particles.

4.1.2 Meshing

LUSAS 6 noded triangle, TAX6 (Figure 4.4(a)), and 8 noded quadrilateral, QAX8 (Figure 4.4(b)), 2D continuum axisymmetric solid elements with quadratic shape functions were used for regular and irregular meshing of the axisymmetric unit cell models. Detailed information on TAX6 and QAX8 is given in Appendix 2. The investigated irregularly and regularly meshed quadrilateral axisymmetric solid (QAX8) models with 108 elements are shown in Figure 4.5(a) and (b), respectively. At the locations where meshing with quadrilateral axisymmetric element was not possible, the program automatically utilized triangle axisymmetric solid (TAX6) elements as depicted in Figure 4.5(a). Since the QAX8 has 4 Gauss points, the regular mesh model has 432 and irregular mesh model has 422 Gauss points. Figure 4.6(a) and (b) show irregularly and regularly meshed triangular element models. The number of elements in these models is 150 (450 Gauss points) and 206 (618 Gauss points) for regular or irregular mesh models respectively. The number of elements (also Gauss or integration points) in irregular mesh model at the particle-matrix interface are increased intentionally in order to model the stress and strain distribution as fine as possible.

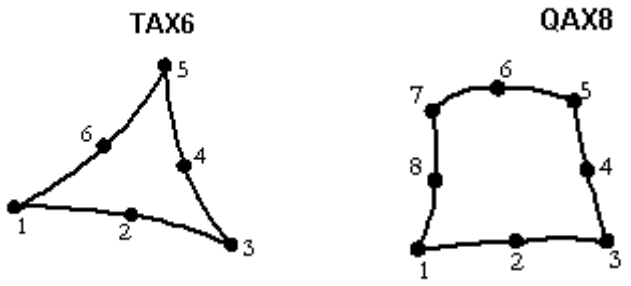

Figure 4.4. LUSAS; **a)** TAX6 (6 nodes) and **b)** QAX8 (8 nodes) axisymmetric elements.

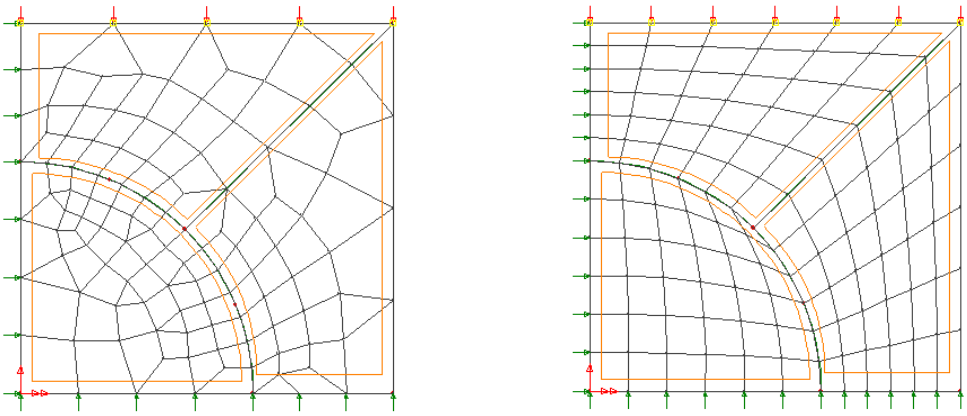

(a) **(b)**

Figure 4.5. Quadrilateral axisymmetric unit cell solid elements with **a)** irregular and **b)** regular meshes.

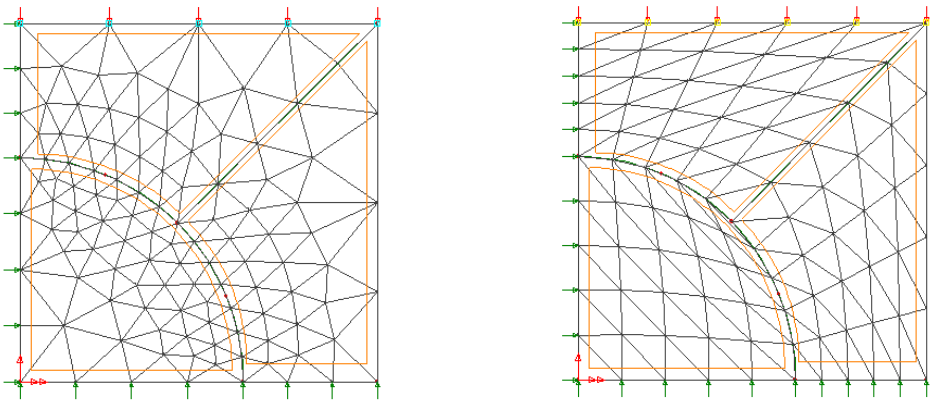

(a) **(b)**

Figure 4.6. Triangle axisymmetric solid element mesh models **a)** irregular and **b)** regular.

Since plasticity calculations take place at the finite element integration points, it is important to consider the integration (or Gauss) point density when meshing the model. Although, fully integration uses multiple points (Figure 4.7(a)) reduced, integration uses limited number of points or single point (Figure 4.7(b)) in integration. Reduced integration elements will require a more refined mesh than fully integrated elements. Therefore, fully integrated elements are used in the unit cell.

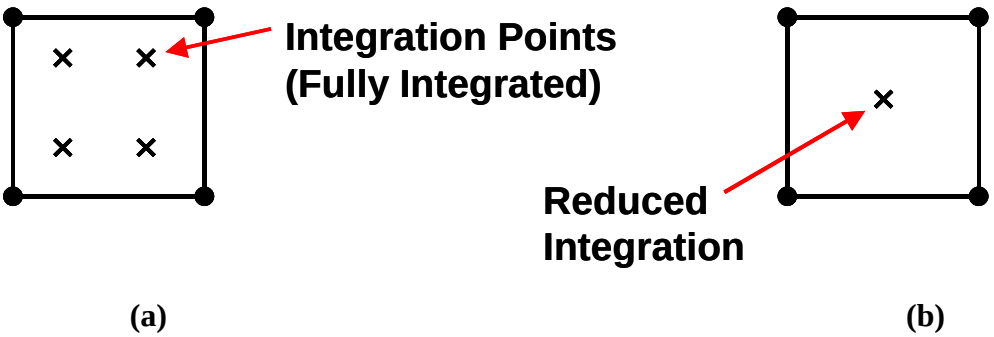

Figure 4.7. (a) Fully integrated element with 4 integration points and **(b)** reduced integrated element.

4.1.3. Boundary conditions

The meshed unit cell with boundary conditions is shown in Figure 4.8. Due to the symmetry, the left edge of the unit cell is fixed on the x-direction: dx=0, and bottom edge is fixed on the y-direction: dy=0. Top edge is constrained on the y-direction: dy/y=0 for geometrical fitting [7,11,12]. There are two possibilities that can be applied to the right edge of the cell [12]. The first one is to unconstraint the right edge so that outer sidewall of the cell will not remain straight after deformation. This is shown in Figure 4.9(b) for 20% total final strain in the y-direction. The second possibility is to constrain the right edge in the-x direction (dx/x=0) so that the right edge will remain flat after the deformation as shown in Figure 4.9(c) for applied 20% total final strain in the y-direction. The condition that the circular cylindrical cell remains circular cylinder comes from enforcing geometric compatibility for a uniform array of fibers perfectly aligned with tensile axis [12]. In our analyses, the unconstrained model is adopted and an example of constrained model is also investigated. Numerical calculations for various particle fractions were conducted on the unconstrained model and calculations with constraint model were only conducted for 15% particle reinforced composite.

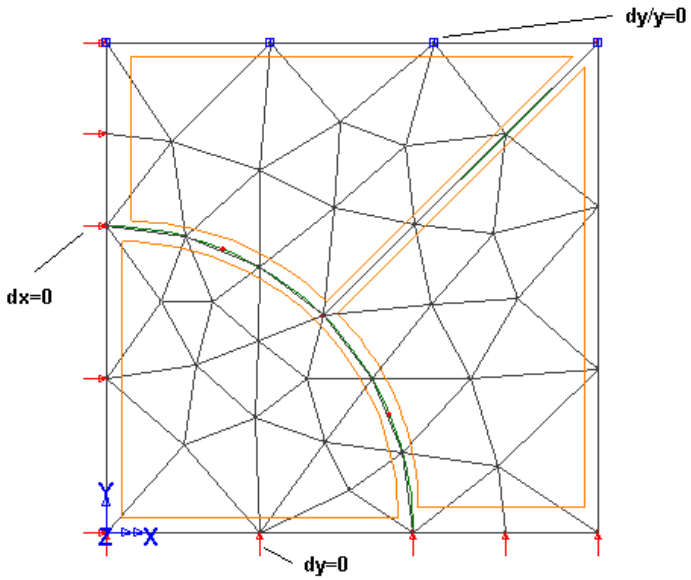

Figure 4.8. Meshed unit cell model and boundary conditions applied.

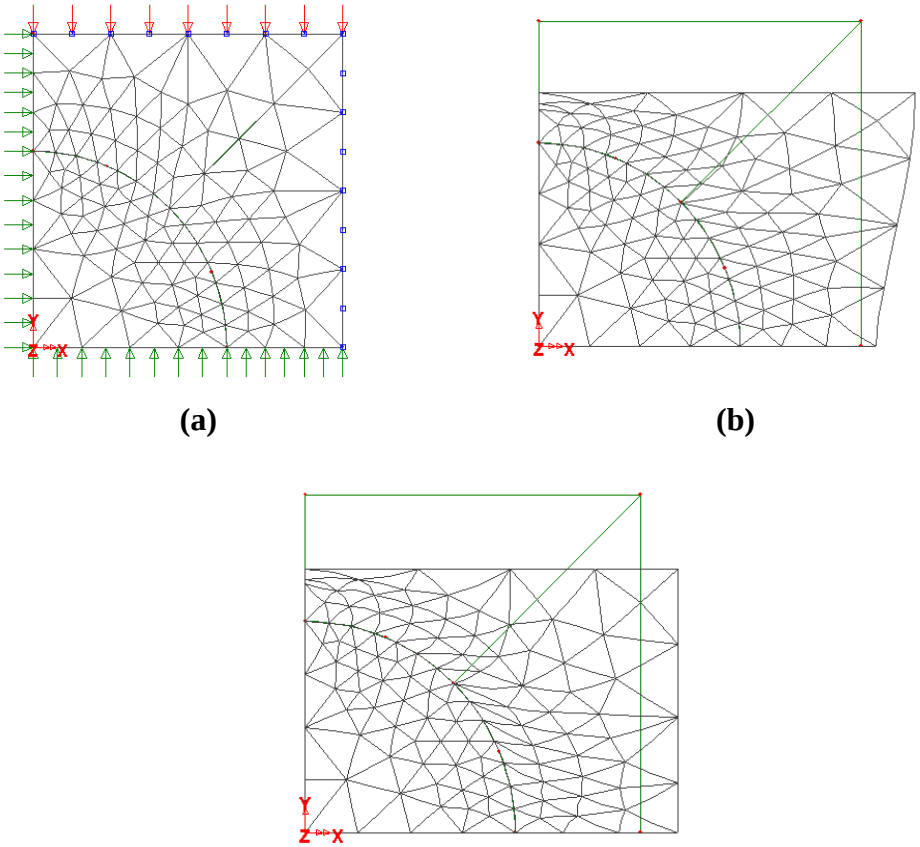

(a) **(b)**

(c)

Figure 4.9. a) Undeformed unit cell model, **b)** unconstraint deformed mesh at 20% strain and **c)** constrained unit cell model deformed until 20% strain.

4.1.4. Calculation Methods

Uniaxial loading of the model was simulated by imposing an incremental displacement in the y-direction. Two displacement increments are applied in two different load cases. Increments of 0.002% and 1% are applied until and after 1% displacement respectively. The deformation of the composite was modeled using von-Misses theory of plastic flow of the 2024-O Al and elastic properties of the SiC reinforcement. The flow stress-strain behavior of the matrix corresponding to the studied strain rate was entered to the program. The elastic modulus of the SiC reinforcement was taken as 450 GPa [24].

The macroscopic stress was calculated using,

$$\sigma_{Ci} = \frac{\sum_{j=1}^{N} \sigma_j}{N} \tag{4.2}$$

where σ_{ci} is the average composite stress at i^{th} increment, σ_j is the element stress at the Gauss points and N is the total number of Gauss points. Macroscopic strain was calculated using,

$$\varepsilon_i = \ln \frac{l_i}{l_o} \tag{4.3}$$

where i is the increment number and l is the final and l_o is the initial length of the unit cell.

4.2. Model Material

The modeling results were compared with a SiCp reinforced 2024-O Al MMC compression behavior at quasi-static and high strain rates. The composite was manufactured by stir casting and its microstructure is shown in Figure 4.10. The average particle size was 30 μm but the particle size ranges between 10 to 50 μm. The average matrix grain size was 200 μm. Since the particles are pushed by the growing dendrites, they are collected at the grain boundaries (Figure 4.10). The matrix material is a wrought alloy which was exposed to extrusion and cross-rolling. Solution treatment was applied to the alloy in order to simulate cast matrix alloy properties. The heat treatment

process was conducted at 385 ˚C for 3 hours following by cooling to 260 ˚C with a cooling rate of 28 ˚C /hour and cooling in the furnace from 260 ˚C to room temperature.

The composite and matrix quasi-static and dynamic compression behavior was previously investigated by Güden and Hall [22] on small cylindrical specimens (6-10 mm in diameter and 6.6 mm in length) using Instron and Split Hopkinson Pressure Bar techniques. In Instron compression testing, the typical strain rate range involved was around ~10^{-4} to 10^{-3} s^{-1} depending on the specimen dimensions and chosen cross-head speed. High strain rate tests in the SHPB involved strain rates up to 4000 s^{-1}.

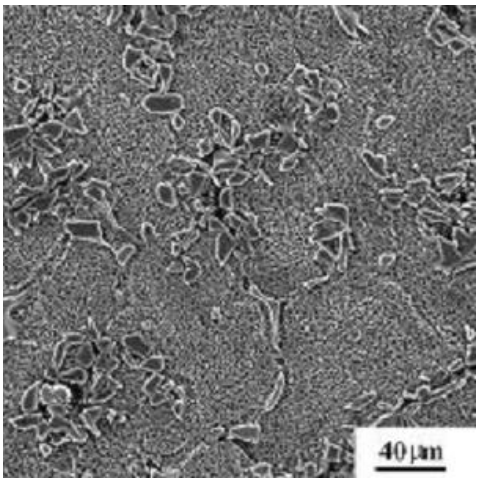

Figure 4.10. SEM micrograph of SiC_p reinforced 2024 Al-O, showing the particle clustering at grain boundaries [22].

4.2.1 Matrix compression properties

The effect of strain rate on the compression behavior of the matrix alloy is shown in Figure 4.11. The flow stress increases with increasing strain rate, showing a strain rate sensitive flow stress behavior.

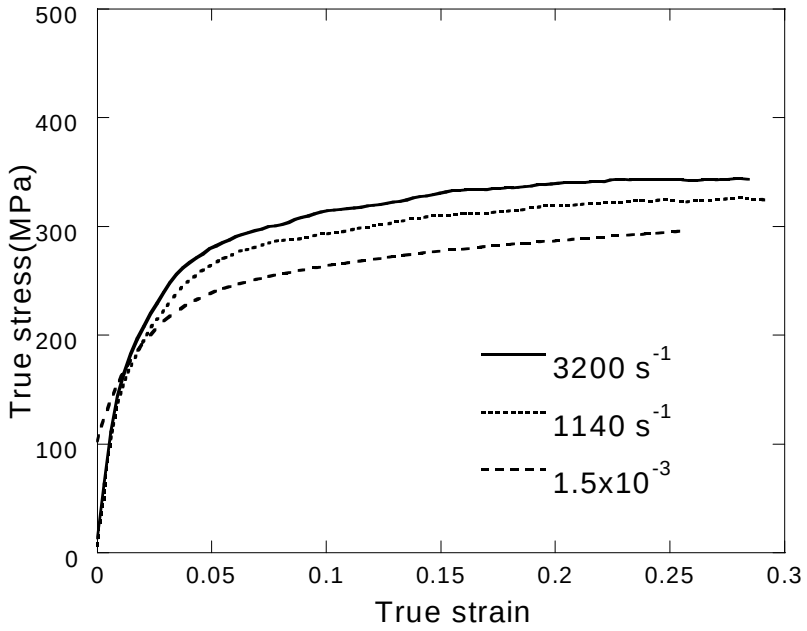

Figure 4.11. True stress-strain curves of the 2024 matrix alloy at various strain rates.

In order to find matrix constitutive equation, the flow stresses of the matrix corresponding 6% strain was extracted and shown as a function of strain in Figure 4.12. The flow stress vs. strain rate data shown in this figure was fitted to the equation:

$$\sigma_D = \sigma_S + k\,\dot{\varepsilon} \tag{4.4}$$

where σ_D and σ_S are the dynamic and reference strain rate flow stresses, respectively. The reference strain rate was 1.5×10^{-3} s^{-1} corresponding to quasi-static strain rates. The high strain rate stress-strain behavior was then calculated by multiplying strain rate sensitivity parameter, k, with the strain rate interested. The value of k was calculated 0.00149 for the matrix alloy. Figure 4.13 shows the calculated stress-strain curves at various strain rates and comparison between experimental and calculated stress-strain curves at 1140 and 3200 s^{-1} strain rates. A good agreement between two in this figure confers that matrix constitutive equation can be simply presented by the Equation 4.4.

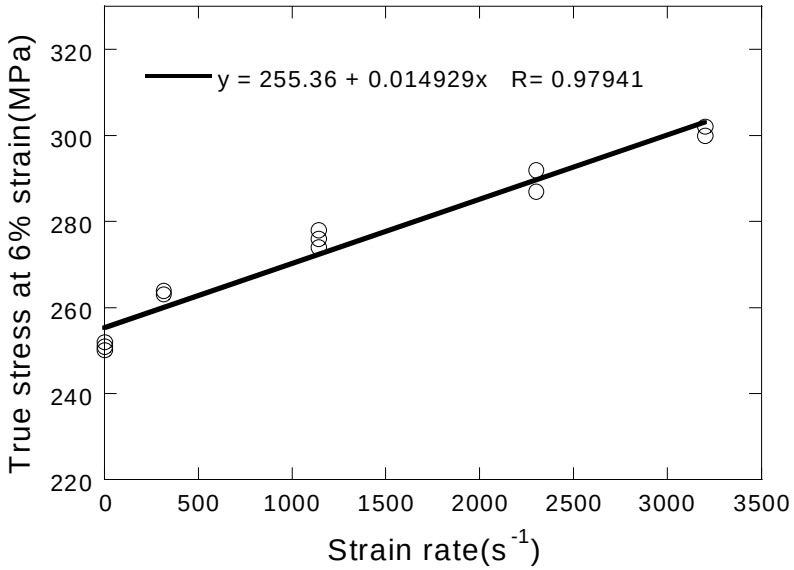

Figure 4.12. Linear fit of the 2024 Al flow stress at 6% strain vs. strain rate curve.

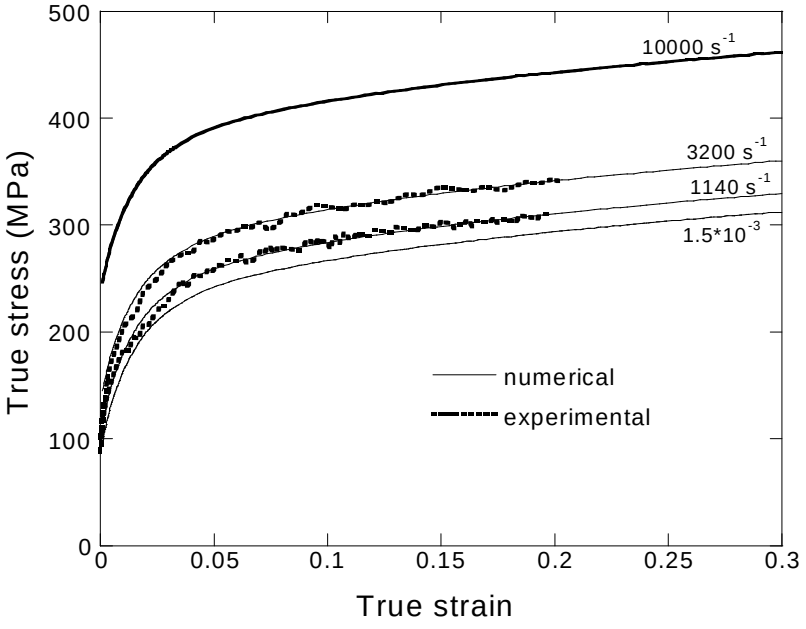

Figure 4.13. Comparison of experimental high strain rate stress-strain curves with the numerical stress-strain curves of Equation 4.4**.**

4.2.2. Metal Matrix Composite

Quasi-static stress-strain curve ($0.0015s^{-1}$) of the composite is shown in Figure 4.14. Initially higher strain hardening and flow stress behavior are observed in the composite. In Figure 4.15, the stress-strain curves of the composite are shown at various strain rates. Similar to the matrix alloy behavior, a strain rate sensitive flow stress behavior is measured.

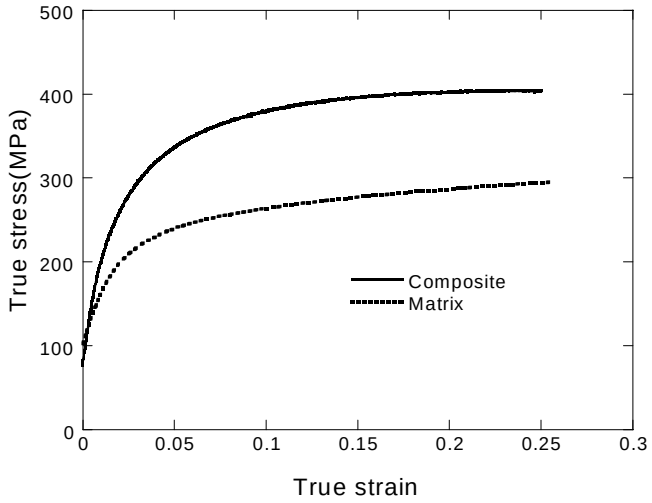

Figure 4.14. Comparison stress-strain curves of matrix and MMC.

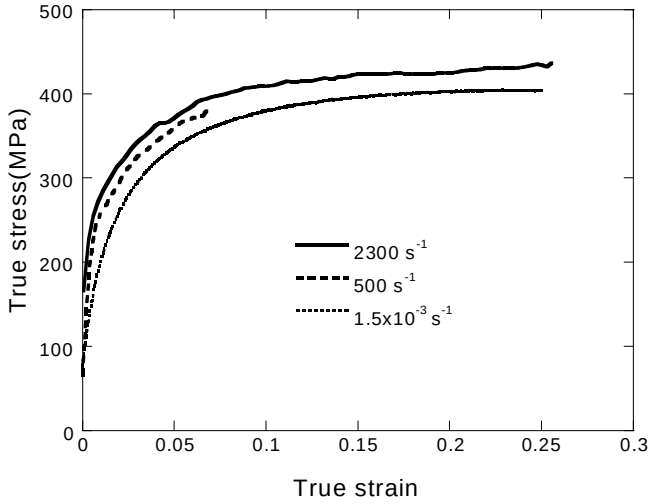

Figure 4.15. True stress-strain curves of the SiCp reinforced MMC at various strain rates.

CHAPTER 5

RESULTS

5.1. Model Parameters

5.1.1. Effect of Element Type and Number

Numerical quasi-static stress-strain curves of four models, regularly and irregularly meshed triangular and quadrilateral solid models (see Figures 4.5 and 4.6), are shown in Figure 5.1 for 15% SiC_p reinforced 2024-O Al composite. In the same figure, quasi-static (0.0015 s^{-1}) experimental stress-strain curve of the composite is also shown for comparison purposes. All models result in lower stresses than composite below 15% strain. It is also noted that regular mesh models give lower stress values than the irregular mesh models. Since the triangular irregular meshing is more flexible and provides relatively fine meshing at particle-matrix interface, it has been chosen for meshing the unit cell models with varying particle fractions.

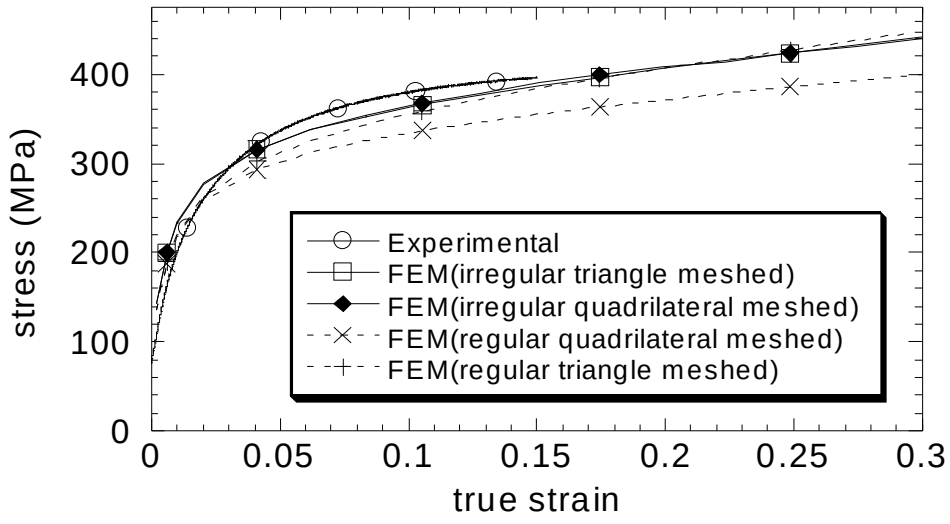

Figure 5.1. Numerical (irregular and regular mesh, triangle and quadratic axisymmetric solid elements models) and experimental stress-strain curves of the 15% SiC_p reinforced Al MMC.

5.1.2. Effect of Boundary Conditions and Mesh Density

Corresponding numerically computed stress-strain curves of the unconstrained and constrained models given in Figure 4.9(b) and (c) are plotted in Figure 5.2. It is found that constraining the right edge results in higher flow stresses and strain hardening in the composite. A similar behavior has been previously found for the modeling of a short fiber composite [12].

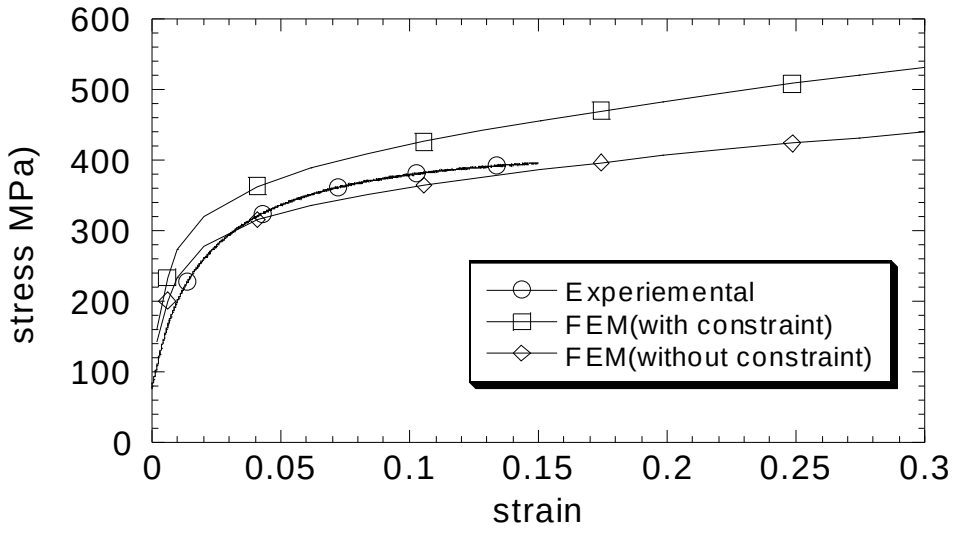

Figure 5.2. Corresponding stress strain curves of the unconstrained and constrained models and experimental stress-strain curve of 15% SiCp reinforced MMC.

To investigate the effect of mesh density, a coarse meshed model (98 elements) of the unit cell (Figure 5.3) is also used in the analysis. It is found that, although fine and coarse mesh models have similar stress values at relatively low strains, at higher strains, the latter results in higher stresses (Figure 5.4). The difference between two also increases as the strain increases.

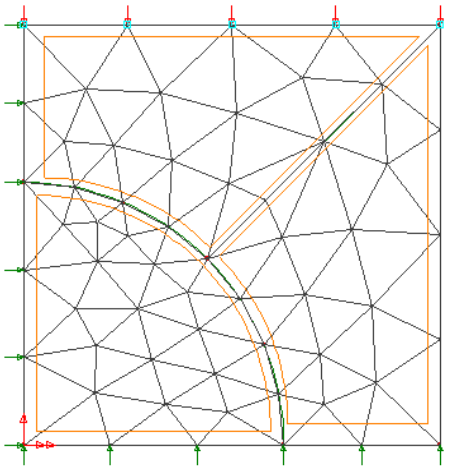

Figure 5.3. Coarse mesh model of the unit cell given in Figure 4.6(a).

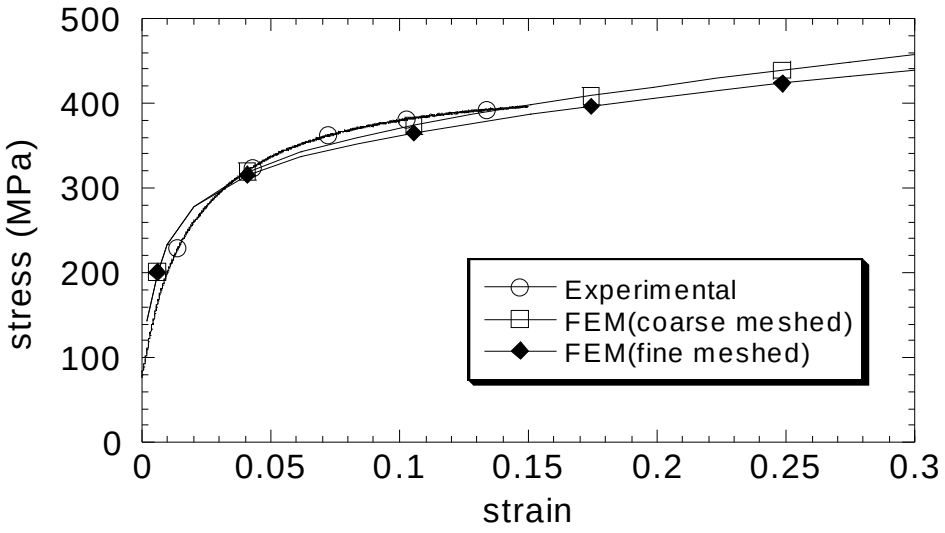

Figure 5.4. Comparison of the quasi-static stress-strain curves of the coarse and fine mesh models of 15% SiCp reinforced MMC.

5.2. Modeling Results

5.2.1. Effect of Volume Fraction

The effect of volume fraction on the composite quasi-static (0.0015 s^{-1}) stress-strain behavior is shown in Figure 5.5. As expected, increase in reinforcement volume fraction (particle size of 30 μm) increases the flow stresses of the matrix. However, increase in the flow stress also depends on the plastic strain. The strain dependent flow stress is shown in Figure 5.6, in which the strengthening (matrix flow stress is

subtracted from composite flow stress) is drawn as function of strain for different particle volume fractions. Linear interpolation to the data in this figure confirms the highest strengthening and strain hardening in 25% of the particle reinforced composite.

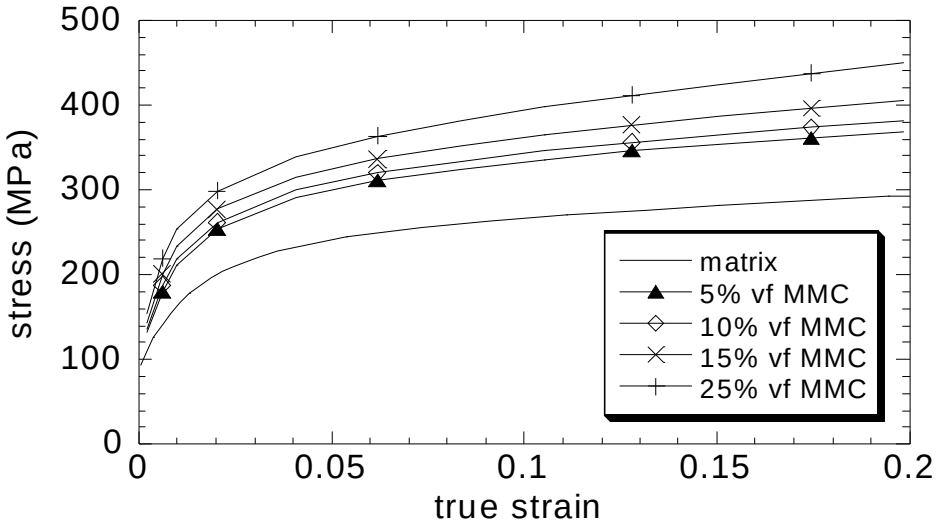

Figure 5.5. Quasi-static true stress-strain curves of 5-10-15-25 % SiC_p reinforced MMC.

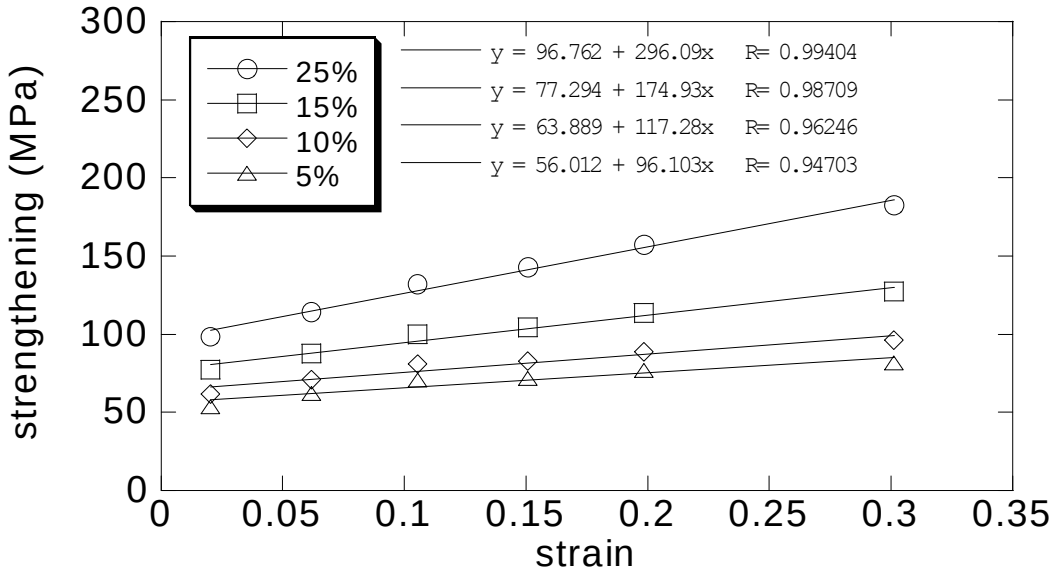

Figure 5.6. Strengthening vs. strain for different volume percentages of particles.

5.2.2. Effect of Strain Rate

Numerical stress-strain curves of the composite at 1500 and 3200 s^{-1} are shown in Figure 5.7 and 5.8 respectively, for different particle volume percentages. Strain rate sensitive flow stress behavior of the composite is clearly seen in these figures. The flow stress of 25% particle reinforcement at 3200s^{-1} is over 500 MPa at 20% strain, while at the same strain it is slightly less than 500 MPa at 1500s^{-1}. In Figures 5.9, 5.10 and 5.11 the strain rate dependent composite flow stress-strain behaviors are shown sequentially for 5, 10 and 25% particle reinforcement. It is noted in these figures that the increase in flow stress is also function of strain. The rate sensitivity of the composite at a specific strain is calculated by plotting on a graph corresponding to flow stresses as function of strain rate, which is shown in Figure 5.12 at 5% strain. Linear interpolation to the data on this figure gives the strain rate sensitivity as a function of particle volume fraction. In Figure 5.12 the highest rate sensitivity is found in 25% particle volume fraction (0.02007) and the smallest rate sensitivity in 5% composite (0.018139). The rate sensitivity of the matrix alloy (0.0149) is less than the composite rate sensitivity.

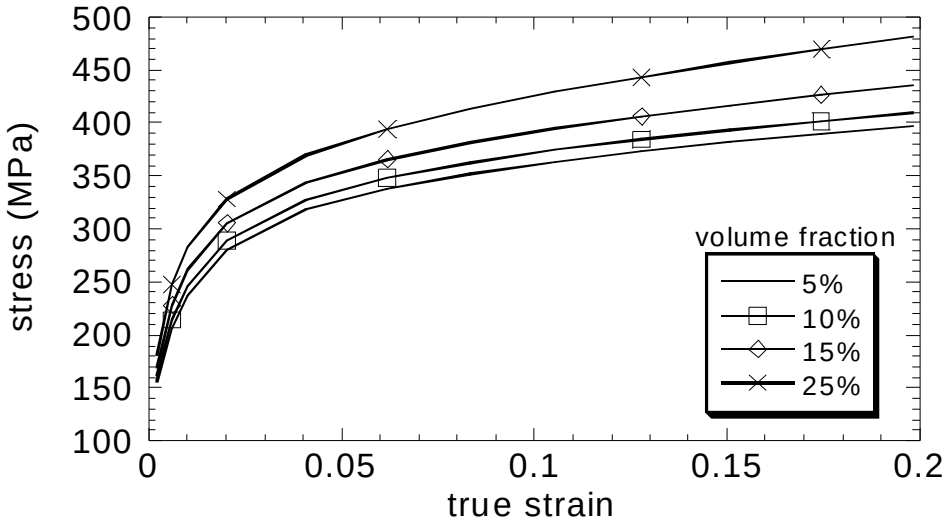

Figure 5.7. Calculated true stress-strain curves of 5, 10, 15 and 25% SiC_p reinforced MMC for 1500 s^{-1} strain rate test.

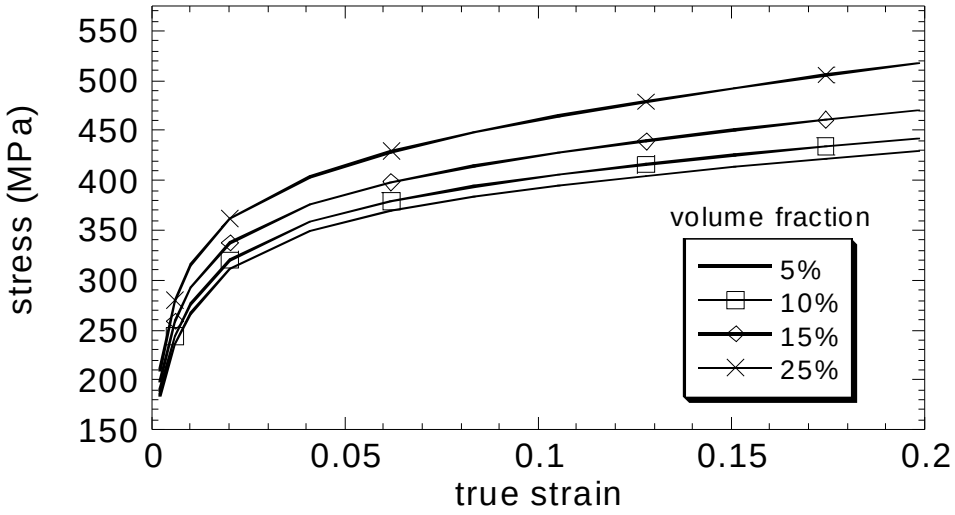

Figure 5.8. Calculated true stress-strain curves of 5, 10, 15 and 25% SiC_p reinforced MMC for 3200 s^{-1} strain rate test.

.

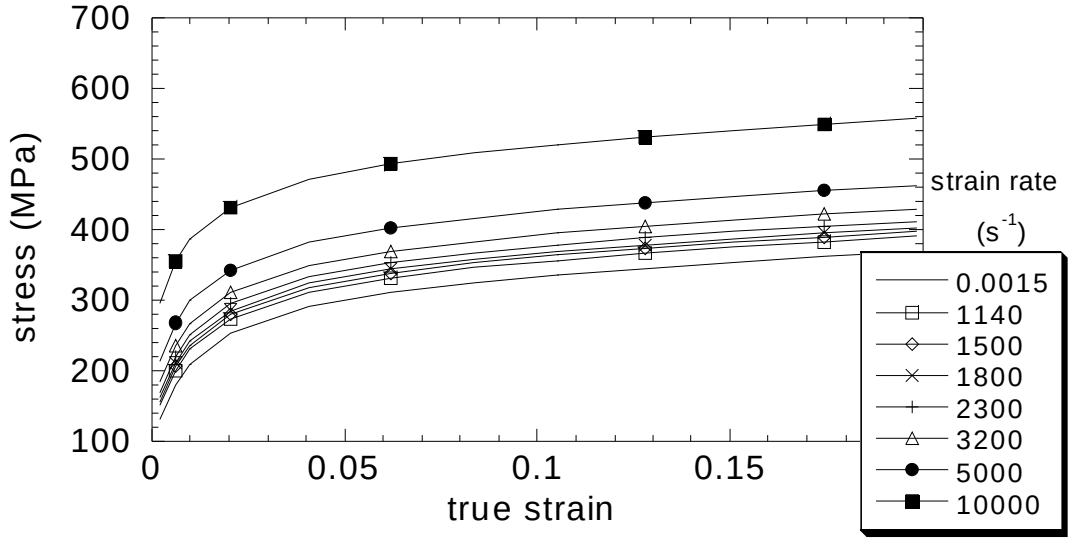

Figure 5.9. Calculated quasi-static and high strain rate stress-strain curves of the 5% SiC_p reinforced MMC.

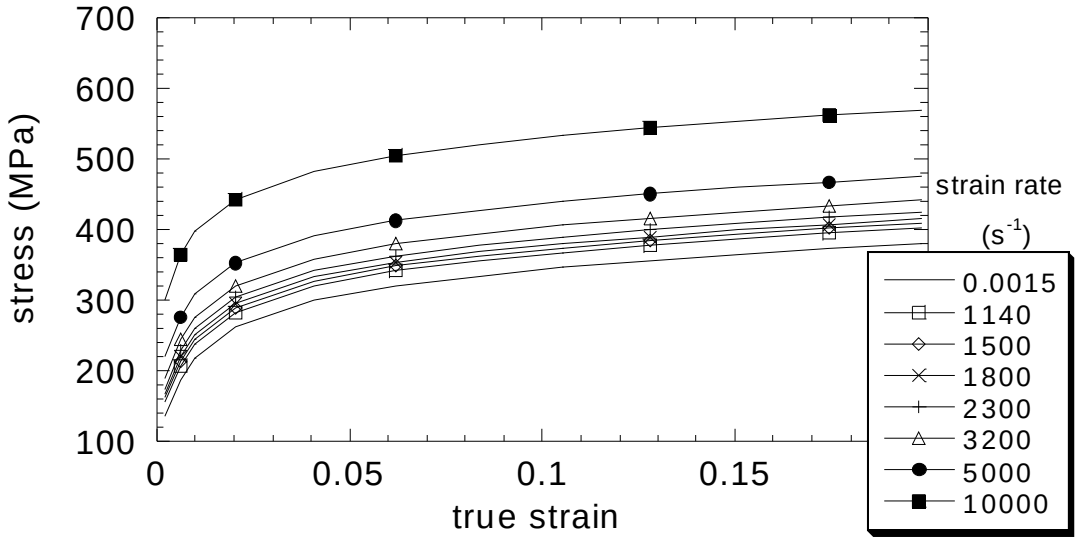

Figure 5.10. Calculated quasi-static and high strain rate stress-strain curves of the 10% SiC_p reinforced MMC.

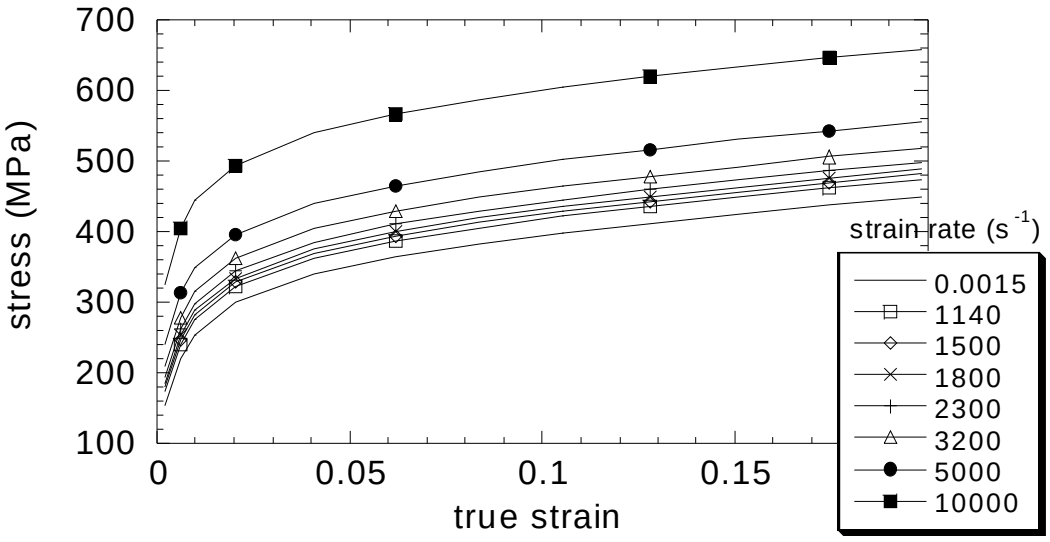

Figure 5.11. Calculated quasi-static and high strain rate stress-strain curves of the 25% SiC_p reinforced MMC.

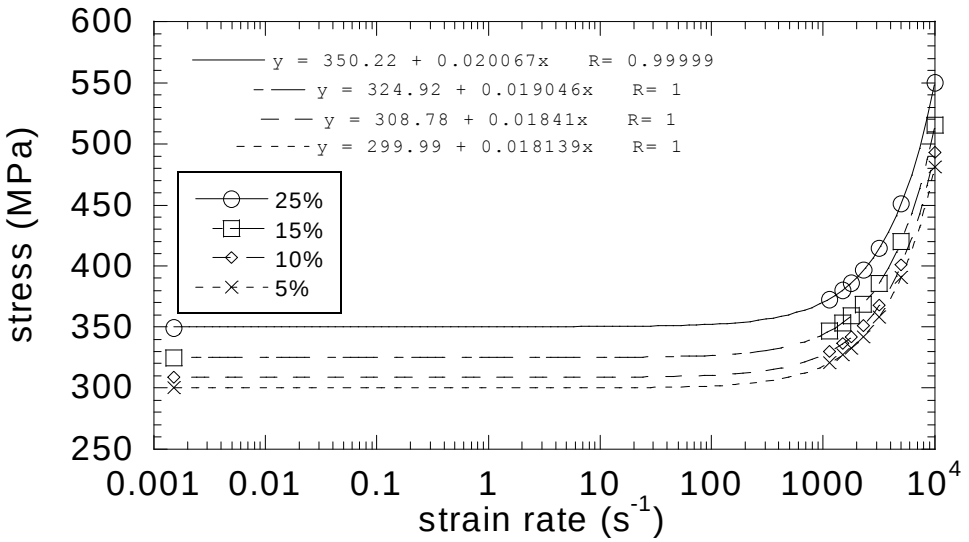

Figure 5.12. Stress *vs.* strain-rate for different volume fractions at 5% strain

The strain rate sensitivity parameters, k and σ_o given in Equation 4.4 were calculated as function strain for the studied particle volume percentages and matrix material and tabulated in Table 5.1. On the same table, the values of k and σ_o of the 15% particulate reinforced MMC with constrained model are also shown. The rate sensitivity of the composite is higher than the matrix alloy for all particle volume fractions studied. The higher strain rate sensitive behavior of the composite also continues at larger values of the strain (Table 5.1). Contrary to matrix alloy rate sensitivity, composite rate sensitivity increases with increasing strain. It is also noted on the same table, the constrained model gives higher strain rate sensitivities than the unconstrained model. The increase in strain rate sensitivity with strain is also higher in the constrained model.

Table 5.1. Strain rate sensitive behavior of the matrix and 5-10-15-25% volume fraction particle reinforced MMC models, and constrained 15% volume fraction reinforced model.

	matrix		MMC, 5% vf		MMC, 10% vf	
strain	σ_0	K	σ_0	K	σ_0	K
5	244.88	0.014929	299.99	0.018139	308.78	0.01841
10	263.31	0.014929	333.05	0.018444	343.27	0.018684
15	282.1	0.014929	353.54	0.018668	364.87	0.018813
25	292.65	0.014929	368.93	0.018846	381.21	0.018878

Continue Table 5.1.

strain	MMC, 15% vf		MMC, 15% vf+cx		MMC, 25% vf	
	σ_0	K	σ_0	K	σ_0	K
5	324.92	0.019046	374.43	0.021763	350.22	0.020067
10	365.16	0.019525	426.36	0.023103	398.12	0.020621
15	386.93	0.019738	456.73	0.023668	425.58	0.020793
25	406.02	0.019871	483.85	0.023979	450.31	0.020912

5.3. Comparison of Numerical and Experimental Stress-Strain Curves

Numerical stress-strain curves of 15% particle reinforced MMC at increasing strain rates are shown in Figure 5.13. Numerical and experimental stress-strain curves of the composite at quasi-static (0.0015 s^{-1}) and high strain rates (2300s^{1}) is given in Figure 5.14. Since deformation of the composite after 15% strain is inhomogeneous (excessive barreling and shear band formation) as marked by arrows in Figure 5.14, the comparison is made until 15% strain. The flow stress-strain curves of the composite, numerical and experimental are given sequentially in Figure 5.15, 5.16 and 5.17 at 5, 10 and 15% strains. As it is seen in these figures within the studied strain range, the experimental flow stresses are higher than those of numerical ones. The linear interpolation to the flow stress-strain rate curves give the strain rate sensitivity which are tabulated in Table 5.2. It is noted in this table, that both experimental and numerical k values increase as the strain increases at a constant matrix rate sensitivity. However, numerical strain rate sensitivity is found to be higher than experimental one. Further more, the matrix strain rate sensitivity is also higher than the experimental composite rate sensitivity except at 15% strain.

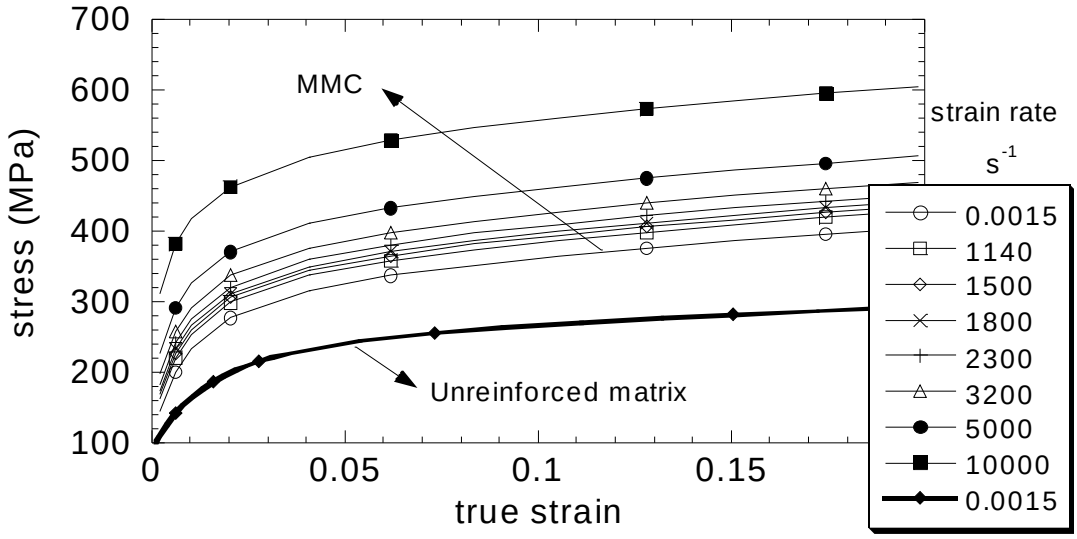

Figure 5.13. Quasi-static and high strain rate stress-strain curves of the 15% particle reinforced MMC and quasi-static stress-strain curve of the matrix.

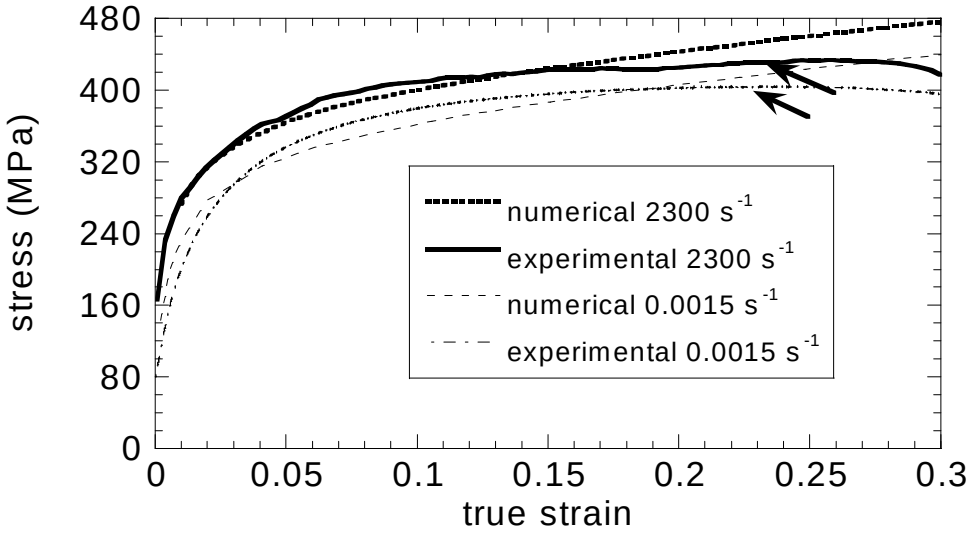

Figure 5.14. Comparison of numerical and experimental quasi-static (0.0015 s^{-1}) and 2300 s^{-1} strain rate stress-strain curves of 15% volume fraction SiCp reinforced MMC.

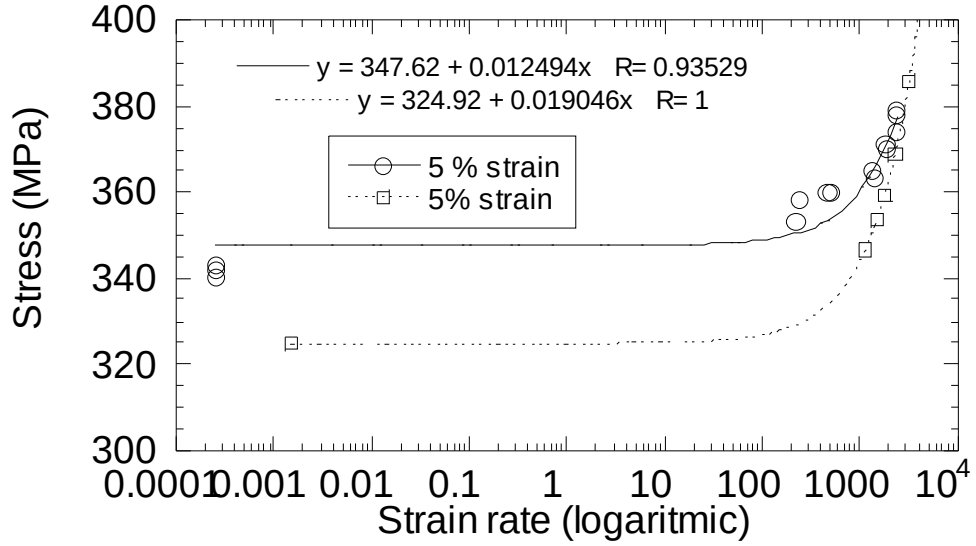

Figure 5.15. Numerical and experimental flow stress at 5% strain vs. strain rate of 15% particle reinforced MMC.

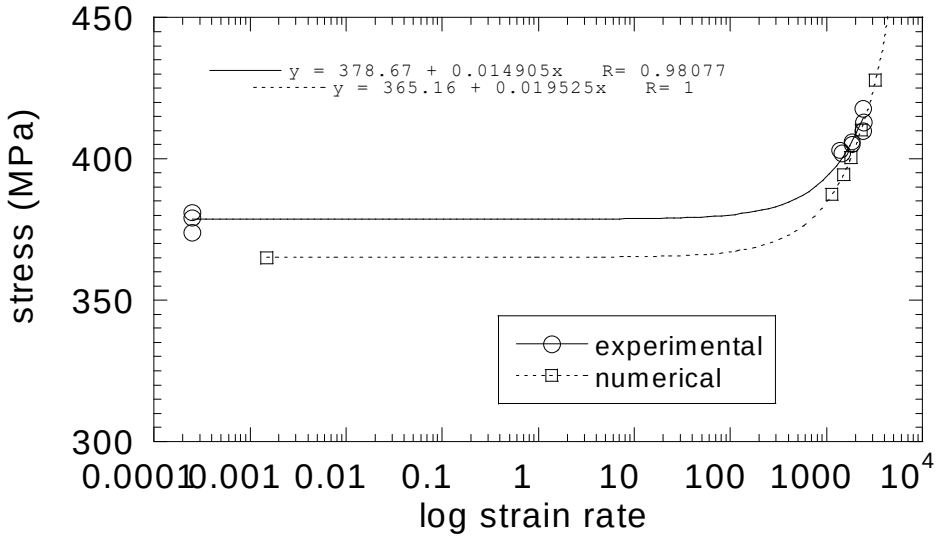

Figure 5.16. Numerical and experimental flow stress at 10% strain vs. strain rate of 15% particle reinforced MMC.

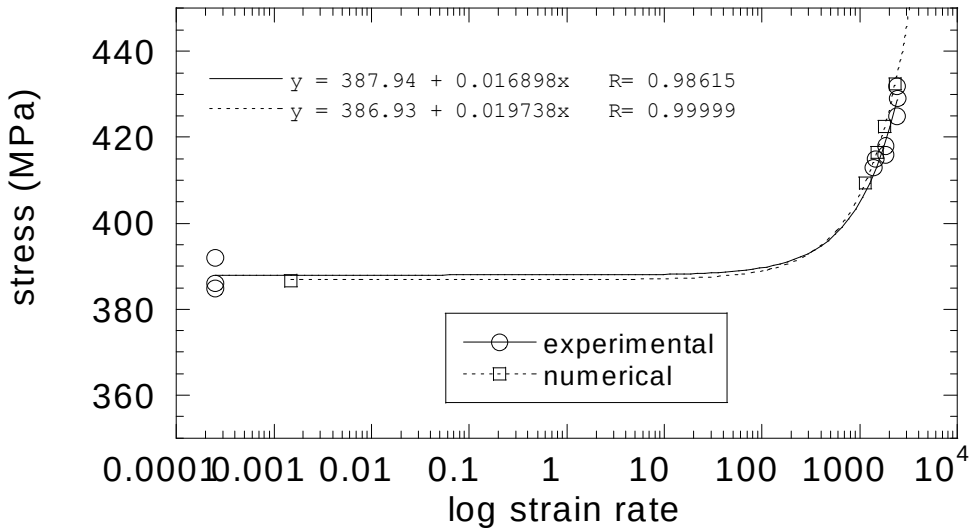

Figure 5.17. Numerical and experimental flow stress at 15% strain vs. strain rate of 15% particle reinforced MMC.

Table 5.2. Calculated and experimental strain rate sensitivity parameters of 15% particle reinforced MMC and matrix alloy.

	matrix		MMC, 15% vf		MMC, 15% vf experimental	
Strain	σ_0	**K**	σ_0	**K**	σ_0	**K**
5	244.88	0.014929	324.92	0.019046	344.96	0.013902
10	263.31	0.014929	365.16	0.019525	378.98	0.014752
15	282.1	0.014929	386.93	0.019738	390.79	0.015503

5.4. Stress-Strain Distribution in the Unit Cell

Using the unit cell model, it is also possible to contour the stresses and strains within the unit cell. Stress distributions in the y-direction for the unconstrained and constrained models are shown sequentially in Figure 5.18.(a) and (b) for 5% particulate reinforced composite at strain of 0.002. The highest compressive stress at the particle-matrix interface is found to be higher than 162 MPa (Figure 5.18(a)) with an average stress of 128 MPa. For the constrained model, the highest stress at the particle-matrix interface is clearly seen at an angle approximately 25° to the loading axis (Y-axis). The

maximum interface compressive stress in the constrained model (>179 MPa) is higher than that with unconstrained model. The stress distribution in the X-direction for both models are also very similar as shown in Figures 5.19 (a) and (b), however, compressive stresses become higher and tensional stresses become smaller in the constrained model. The highest compressive stress is located near to the particle–matrix interface at the upper quarter of the particle. Highest tensile stress is along the particle matrix interface at about 25 degrees to the X-direction. In Figures 5.20 and 5.21, the strain distributions in Y and X-directions are shown for unconstrained and constrained models, respectively. Although average strains for the models are the same, the maximum compressive strain is higher in constrained model in the Y-direction. Similarly, the strain in the X-direction for the constrained model is higher than that of the unconstrained model (Figure 5.21(a) and (b)). Following figures, Figure 5.22 and 5.23 show the stress and strain distribution in 25% particle reinforced MMC for the average strain of 0.002% for the unconstrained model. The particle effect is clearly seen in Figure 5.22(a); the maximum compressive stress increases to 232 MPa and average stress to 148 MPa (see Figure 5.18 for comparison). The stress distribution profile in 25% particle reinforced MMC in X and Y-directions is however similar to that in 5% composite. It is also noted that for both directions, the maximum strains in 25% particle reinforced MMC are higher than those of 5% particle reinforced MMC, although the average strains are the same (0.002%). These results confirm the fact that higher particle volume fractions induce higher maximum stresses and strains in the composite, showing the higher probability of the failure in composites with higher volume fraction particle.

In Figure 5.24(a) and 5.25(a), the stress and strain distributions in Y-direction in 5% particle reinforced MMC are shown sequentially at 5, 10 and 20% strains. As seen in these figures, both maximum stresses and strains at particle-matrix interface increase as the strain increases.

Figure 5.26 shows the equivalent stress distribution in the composite. The maximum stress is 25^{o} to the loading axis and plastic deformation most probably starts at this location.

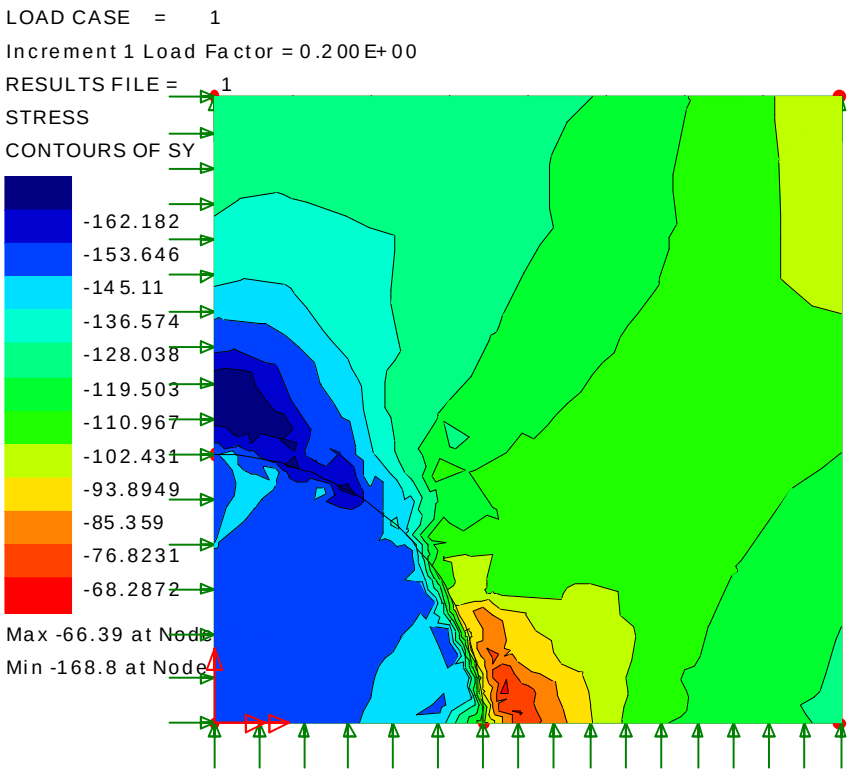

(a)

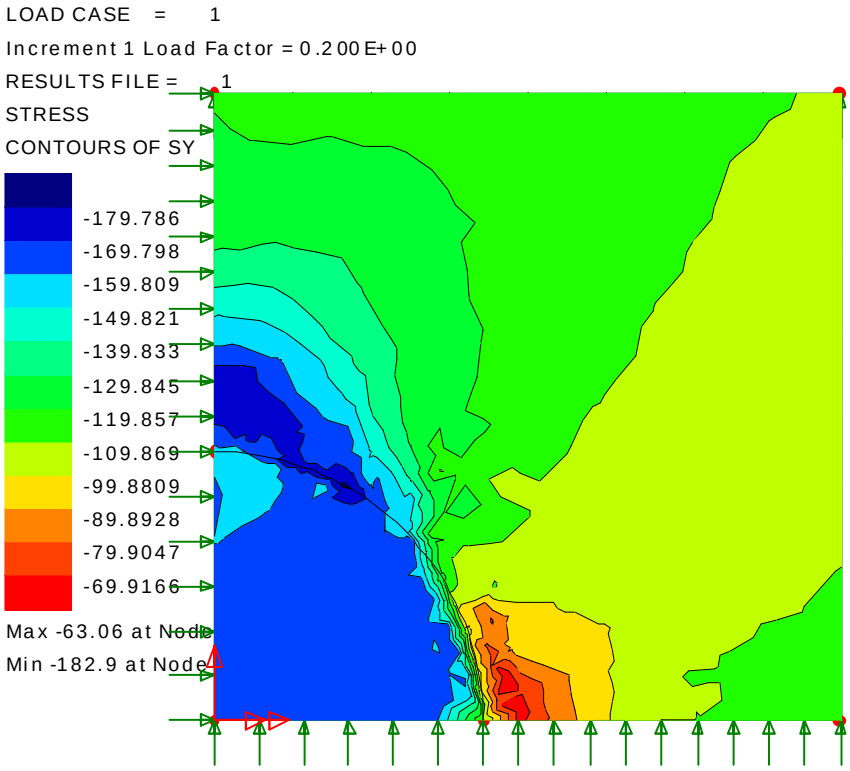

(b)

Figure 5.18. Stress distribution in Y-direction for 5% particle reinforced MMC **a)** unconstrained and **b)** constrained models.

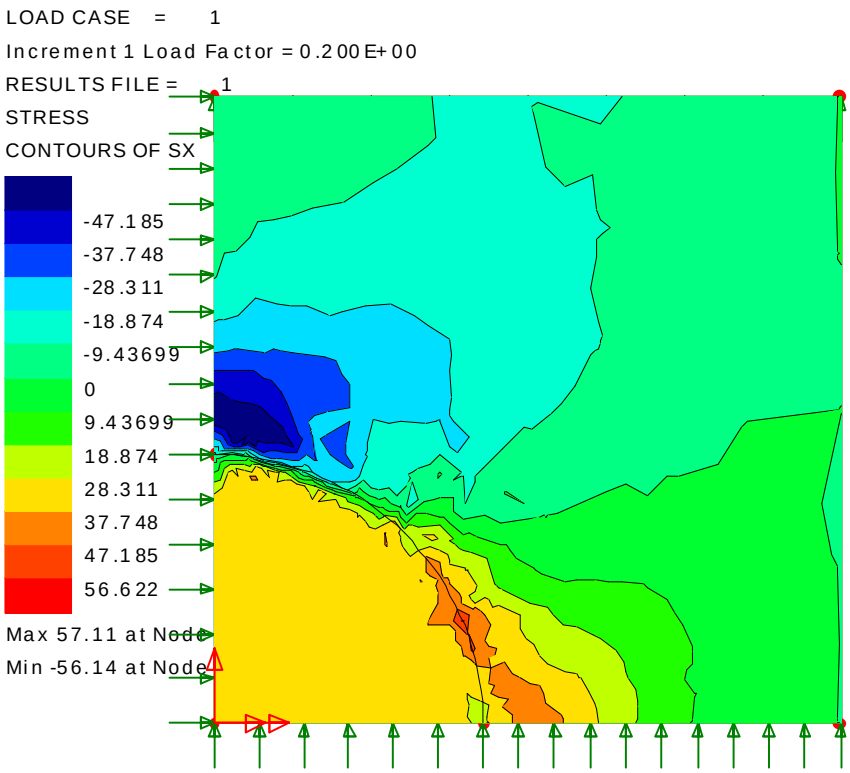

(a)

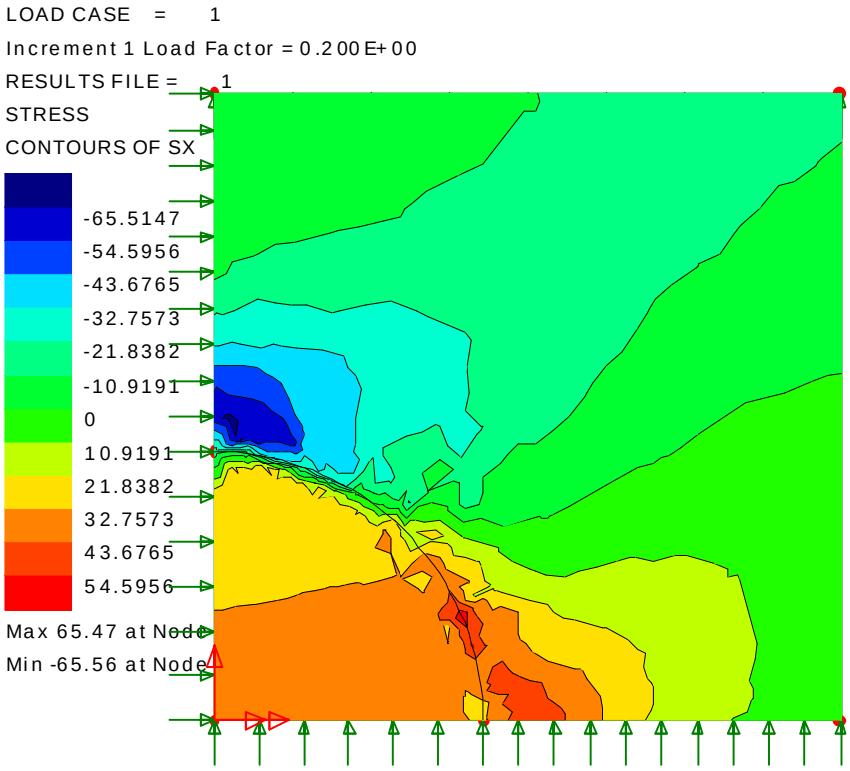

(b)

Figure 5.19. Stress distribution in X-direction for 5% particle reinforced MMC **a)** unconstrained **b)** constrained models.

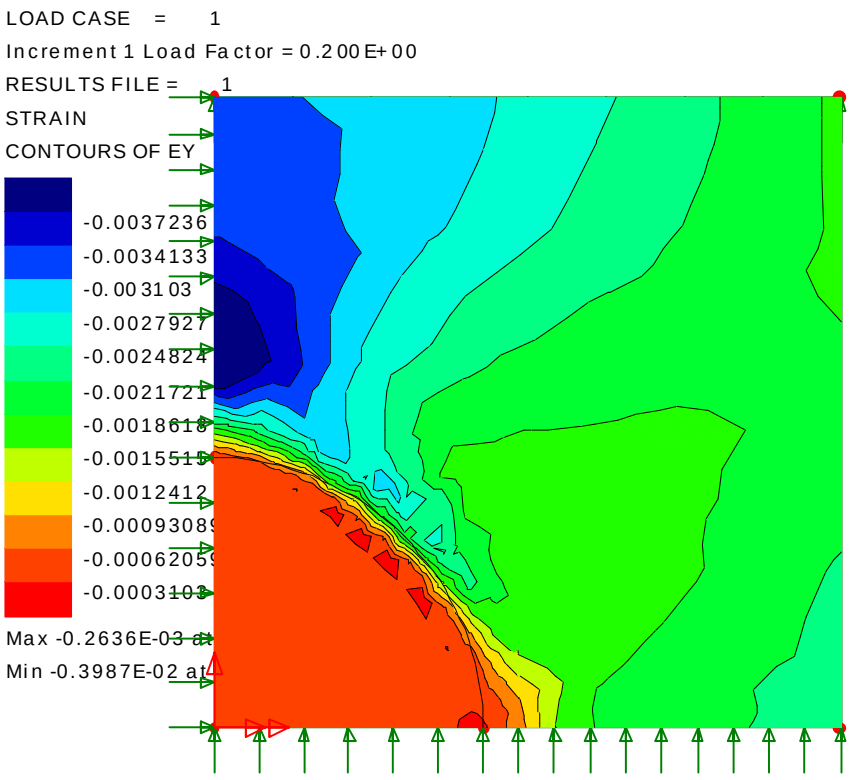

(a)

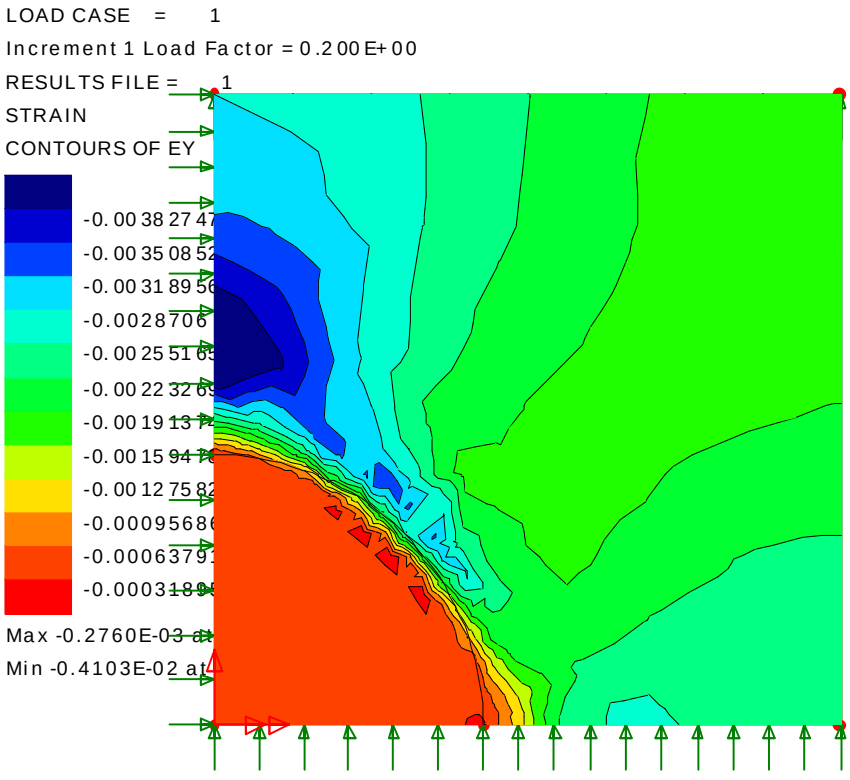

(b)

Figure 5.20. Strain distribution in Y-direction for 5% particle reinforced MMC **a)** unconstrained **b)** constrained models.

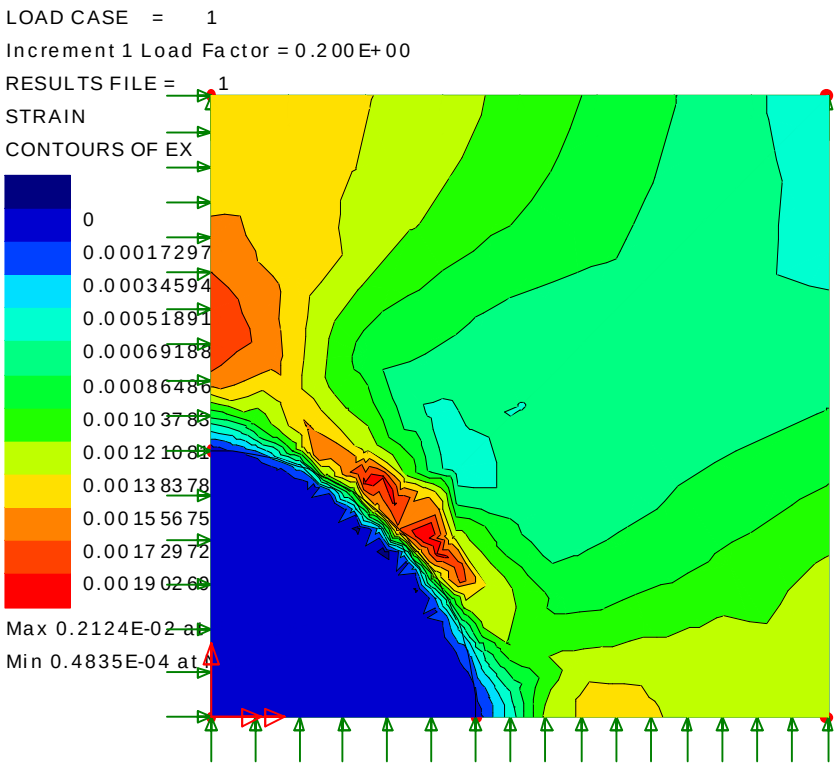

(a)

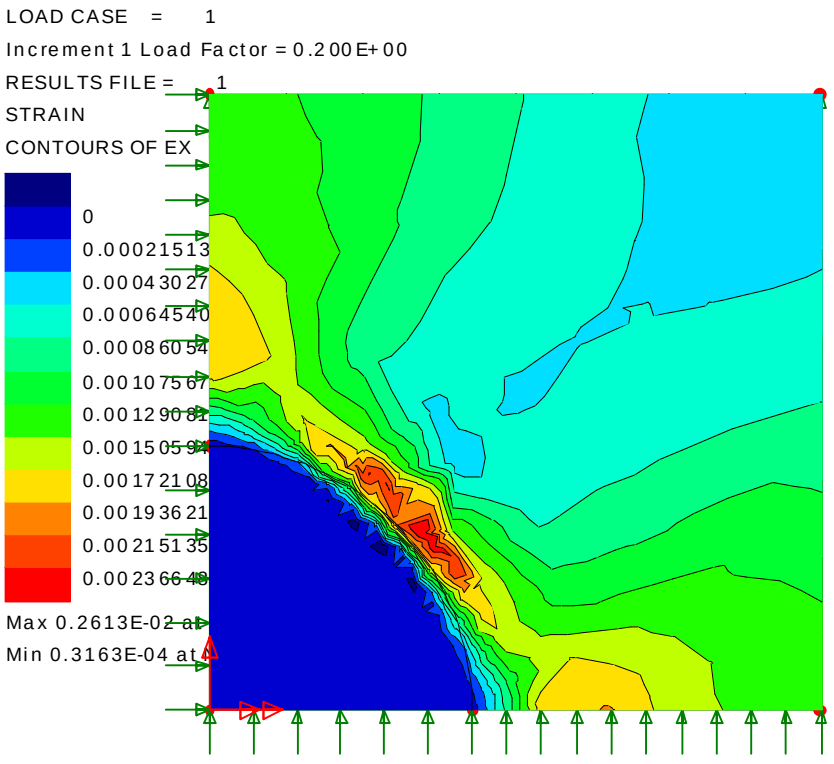

(b)

Figure 5.21. Strain distribution in X-direction for 5% particle reinforced MMC **a)** unconstrained **b)** constrained models.

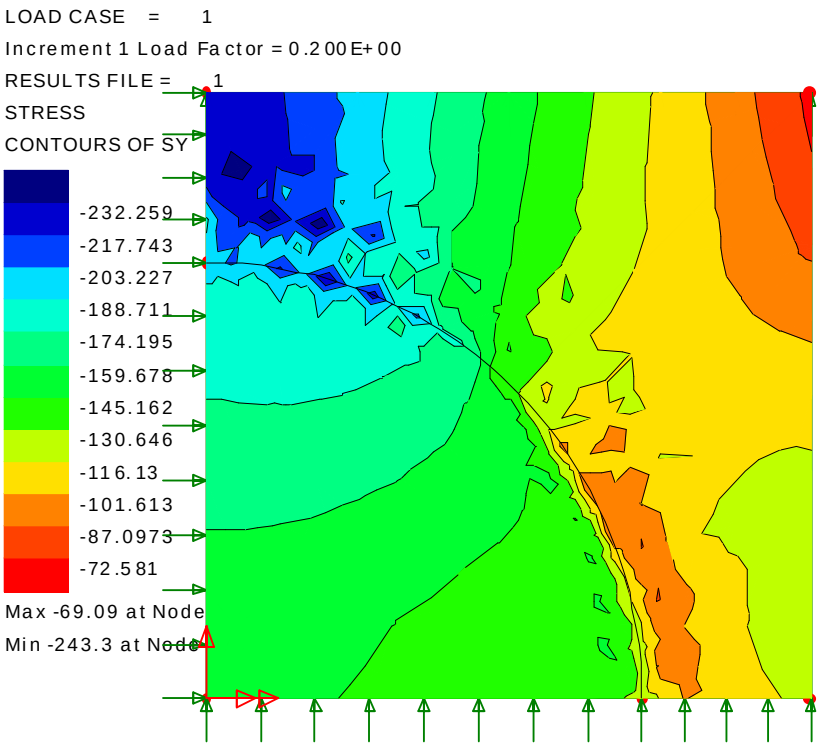

(a)

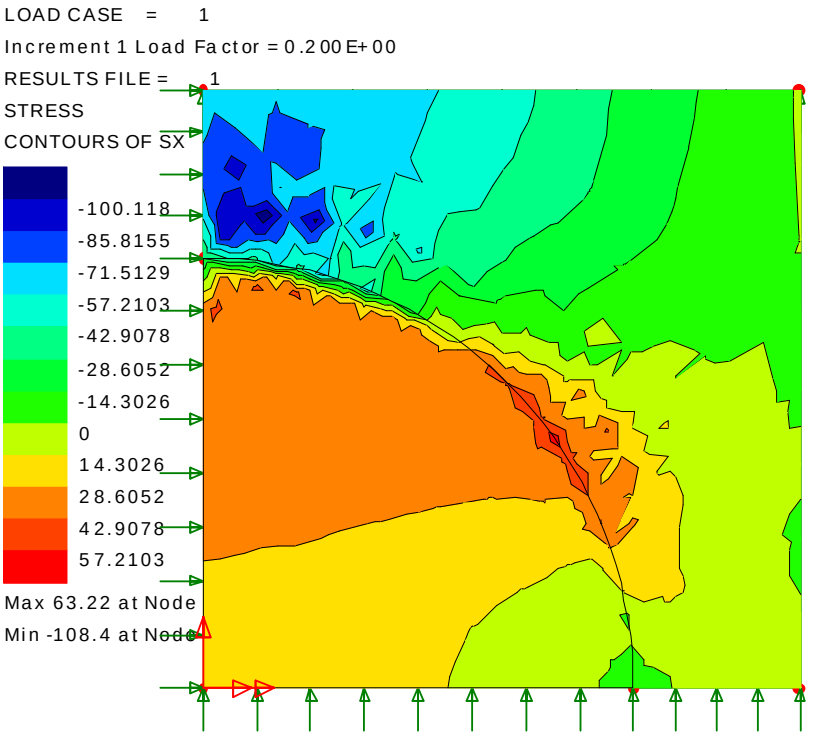

(b)

Figure 5.22. Stress distribution for 25% reinforced MMC **a)** Y and **b)** X direction.

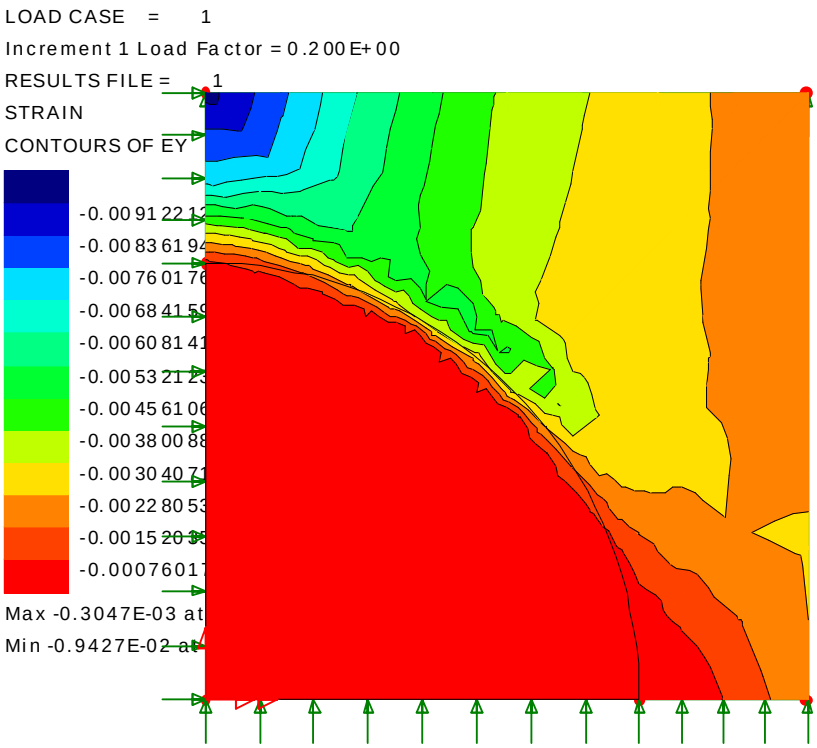

(a)

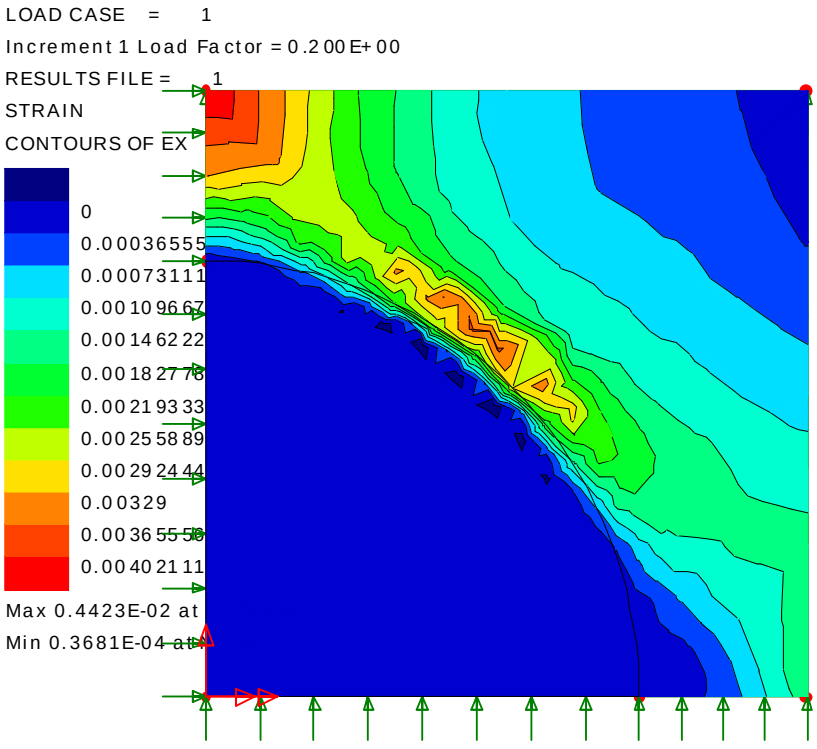

(b)

Figure 5.23. Strain distribution for 25% reinforced MMC **a)** Y-direction **b)** X-direction

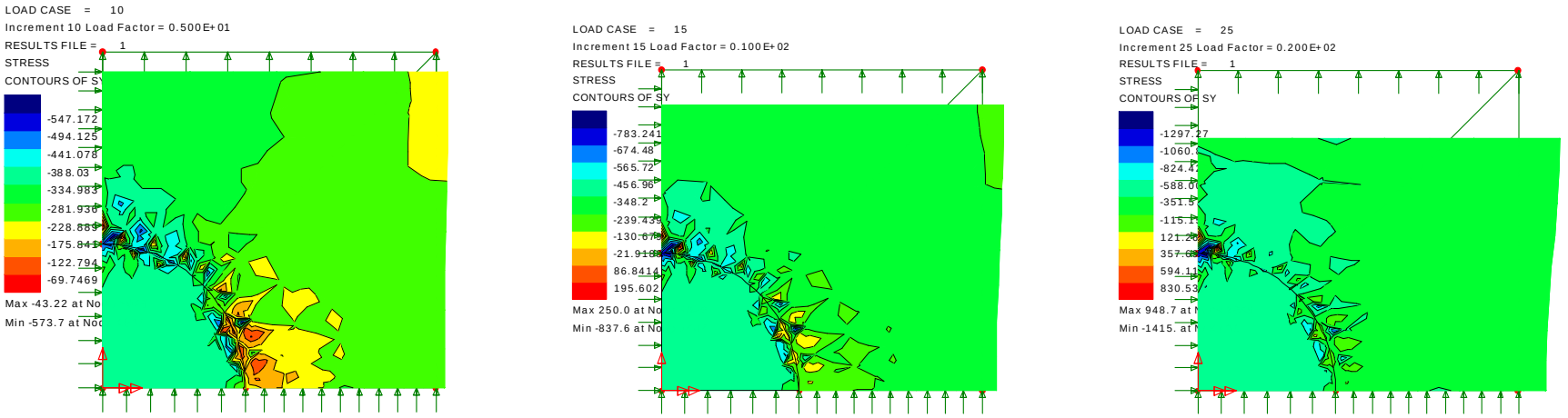

(a) **(b)** **(c)**

Figure 5.24. Stress distribution in Y-direction **a)** 5, **b)** 15 and **c)** 20 % strains for unconstrained model.

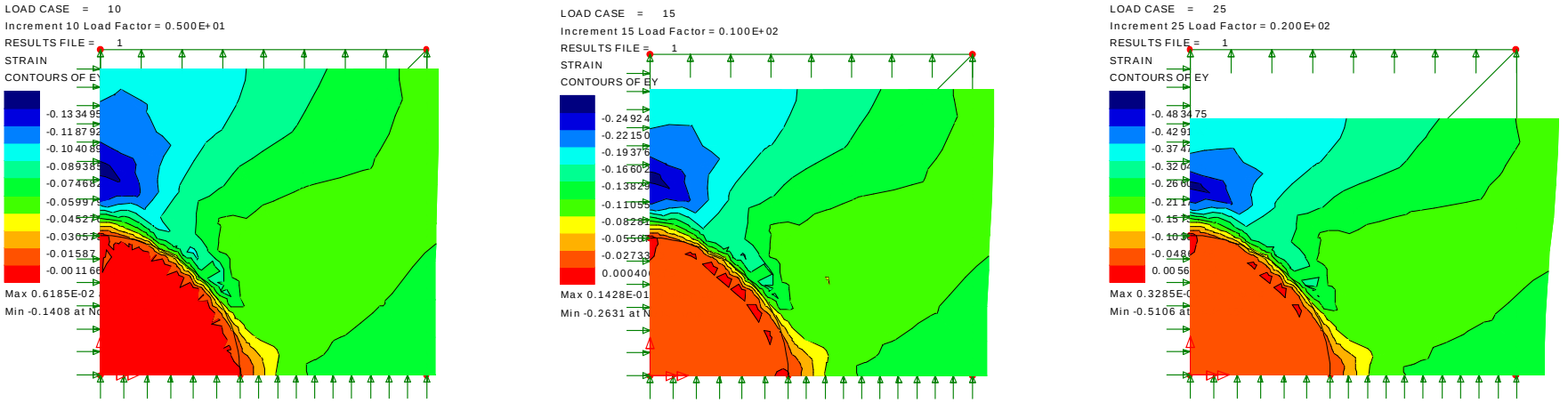

(a) **(b)** **(c)**

Figure 5.25. Strain distribution in Y-direction **a)** 5, **b)** 15 and **c)** 20 % strains for unconstrained model.

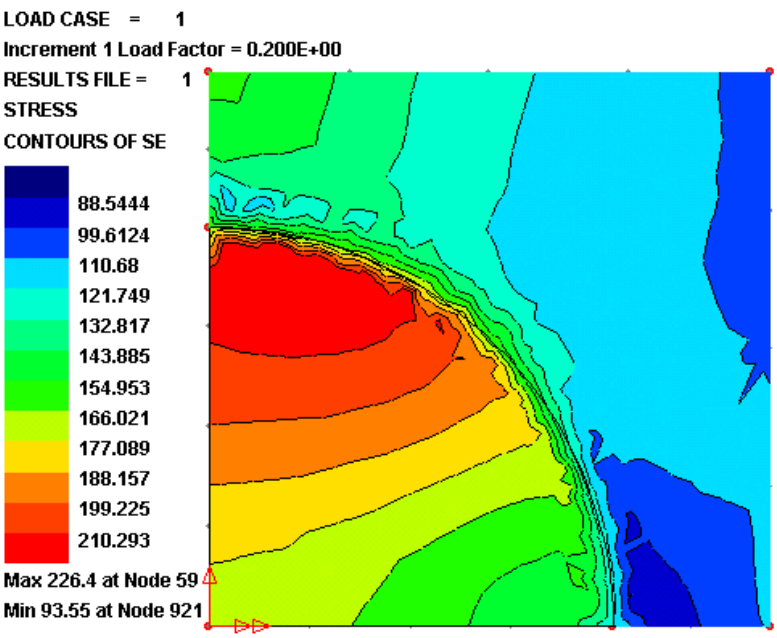

Figure 5.26. Equivalent stress distribution for 25% reinforced MMC, unconstrained model.

The effect of particle corners to the stress-strain curve of the composite was investigated by comparing the unit cell models given in Figure 5.27. The first unit cell in this figure is a cylindrical and the second is a perfectly spherical particle embedded inside the matrix. The unit cells have the same particle percentages, 15%. The corresponding stress-strain curves of the unit cells given in Figure 5.28 show flow stresses and strain hardening rate are higher in the unit cell of cylindrical particle. The stress distribution of two models in the Y-direction is shown in Figure 5.29 for 1 and 10% strains. In the first model, the maximum stresses and the average stress are much higher than those of the second model.

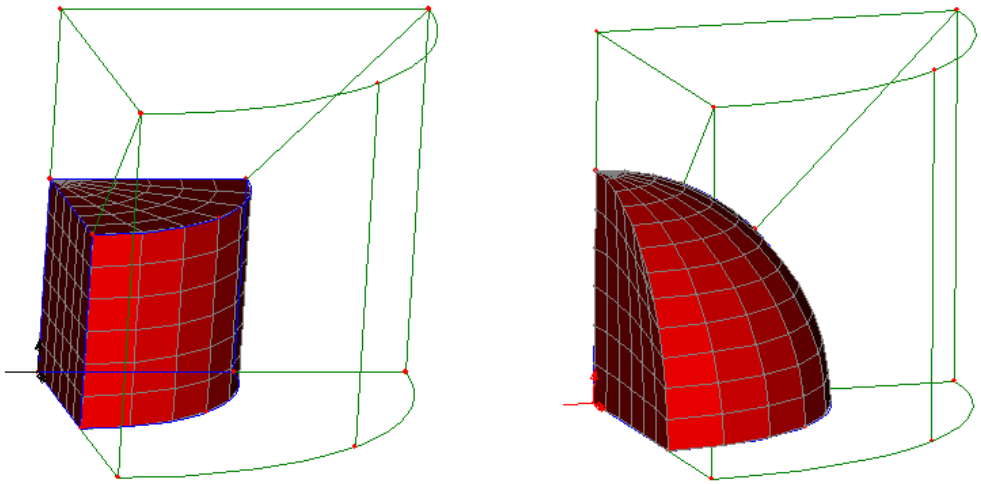

(a) **(b)**

Figure 5.27. a) Cylindrical and **b)** spherical particle reinforced MMC unit cell models.

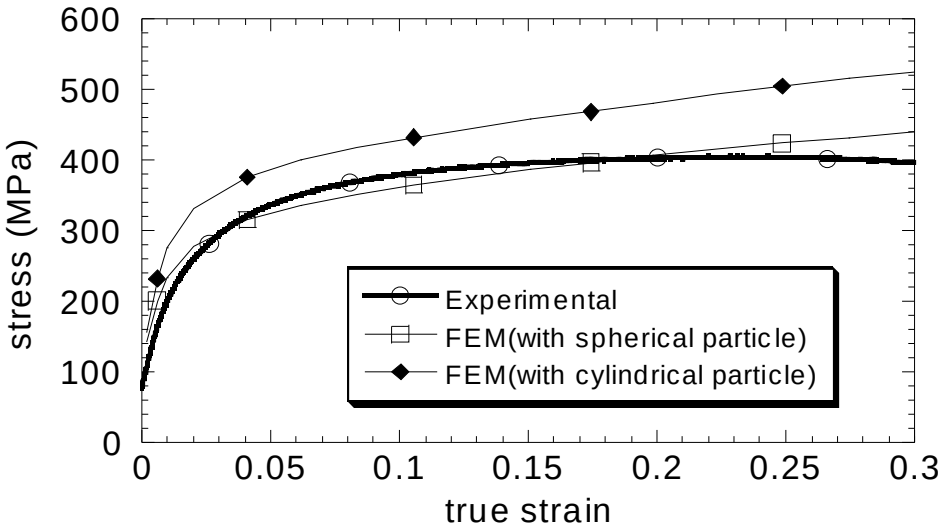

Figure 5.28. Sharp corner strengthening effect.

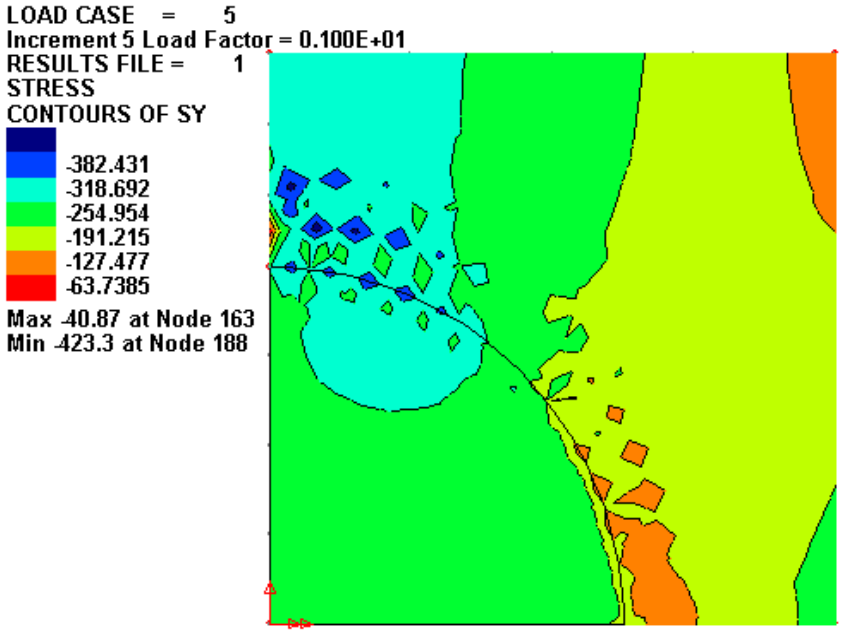
LOAD CASE = 5
Increment 5 Load Factor = 0.100E+01
RESULTS FILE = 1
STRESS
CONTOURS OF SY
-382.431
-318.692
-254.954
-191.215
-127.477
-63.7385
Max -40.87 at Node 163
Min -423.3 at Node 188

(a)

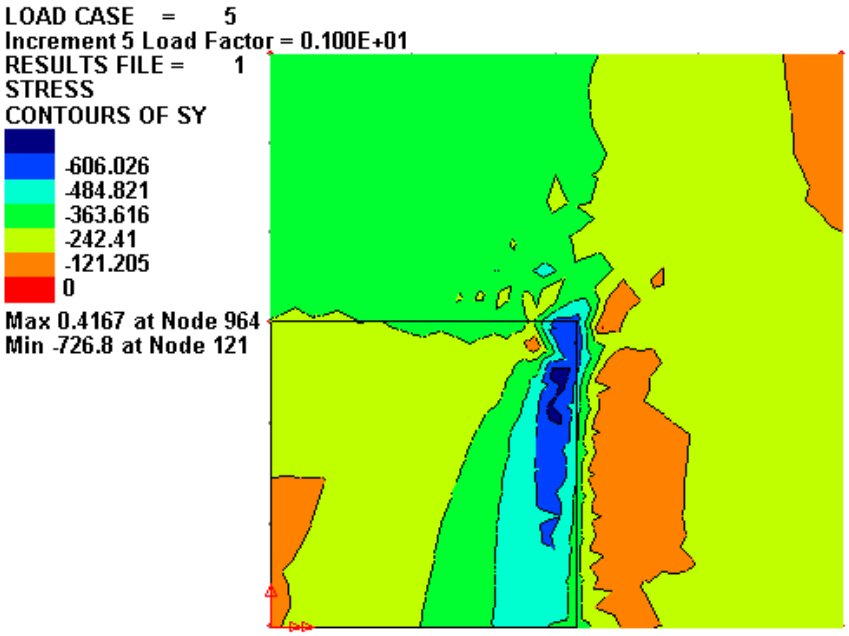
LOAD CASE = 5
Increment 5 Load Factor = 0.100E+01
RESULTS FILE = 1
STRESS
CONTOURS OF SY
-606.026
-484.821
-363.616
-242.41
-121.205
0
Max 0.4167 at Node 964
Min -726.8 at Node 121

(b)

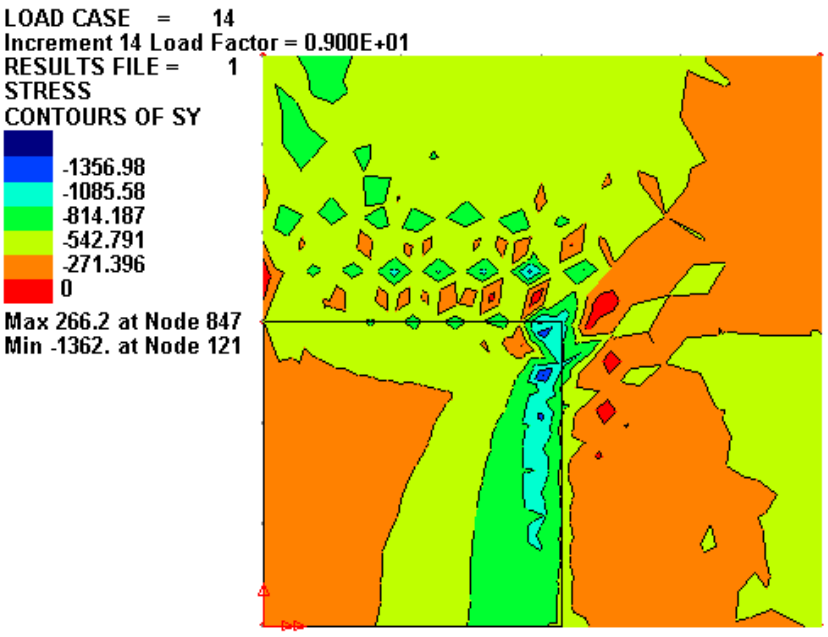

(c)

Figure 5.29. Stress distribution in Y-direction **a)** spherical and b) cylindrical particle MMC at 1% strain and **c)** at 10% strain in cylindrical particle reinforced MMC.

CHAPTER 6

DISCUSSION

6.1. Unit cell model

An increase in the number of elements (mesh density) is known to increases the accuracy of any FE unit cell model. A compromise should however be made between accuracy and program-run time since higher number of elements unavoidably rises the program-run time. The run time for the unit cell model used in this thesis is approximately 30 minutes. This might be increased in order to investigate the effect of number of elements on the accuracy of the results obtained. Since the program is limited to 250 numbers of elements, an investigation over this value could not be possible.

The use of irregular mesh is more appropriate for the structures that contain irregular surfaces and interfaces. Irregularities in geometry including cracks, notches, sharp-cornered particles and interfaces should also be meshed in an appropriate way in order to precisely simulate local variations of stresses and strains around them. These can only be possible with irregular meshing.

The higher stresses developed in the constrained model is obviously due to the development of the internal stresses in order for the right edge of the unit cell to remain flat after the deformation. Although, at low particle volume fractions, this may result in negligible increase in stress values as compared with the unconstrained model, at increasingly high particle volume fractions, the increase in stress values becomes significantly higher, as also shown for the studied model in Figure 5.2. In previous studies, it has been also shown for short and whisker reinforced MMCs that the constrained model resulted in relatively higher flow stresses [12].

6.2. Model Results

6.2.1. Matrix Rate Sensitivity

The effect of strain rate on the flow stresses of the FCC and BCC materials is well documented. Tirupataiah and Sundararajan [31] have represented flow stress *vs*. logarithm of strain rate in two parts, a high strain rate sensitive regime after a transition strain rate, $\dot{\varepsilon}_{tr}$, and a lower strain rate regime below $\dot{\varepsilon}_{tr}$ as schematically plotted in Figure 6.1.

Tirupataiah [32] has further constructed the transition strain rates for a number of metals and alloys as shown in Figure 6.2. As depicted in Figure 6.2, the transition strain rate for common metals and alloys lies between 10^2 to 10^4 s^{-1}. The transition strain rate, as shown in Figure 6.2, decreases as the strength of the metals or alloys increases and it is not affected by the specific metal-alloy system but is only affected by the strength. Before the transition strain rate, it is usually assumed that the deformation is controlled by the thermally activated deformation mechanism [33] and a logarithmic relation between stress and strain rate is usually found in this regime as,

$$\sigma = \sigma_o + k \log \dot{\varepsilon} \tag{6.1}$$

Above the transition strain rate, the flow stress is assumed to be drag controlled [33]. Stress and strain rate in this regime is usually expressed with a linear relation as,

$$\sigma = \sigma_o + k \dot{\varepsilon} \tag{6.2}$$

In order to apply Equations 6.1 and 6.2 to the flow stresses, the experimental flow stresses between quasi-static and high strain rate, 1 and 100 s^{-1}, must also be provided. Using conventional static and dynamic testing methods, the experimentation within this strain rate regime could not be possible. However, the matrix flow stresses of the studied composite material are sufficiently well represented by the Equation 6.2 within the studied strain rate regime.

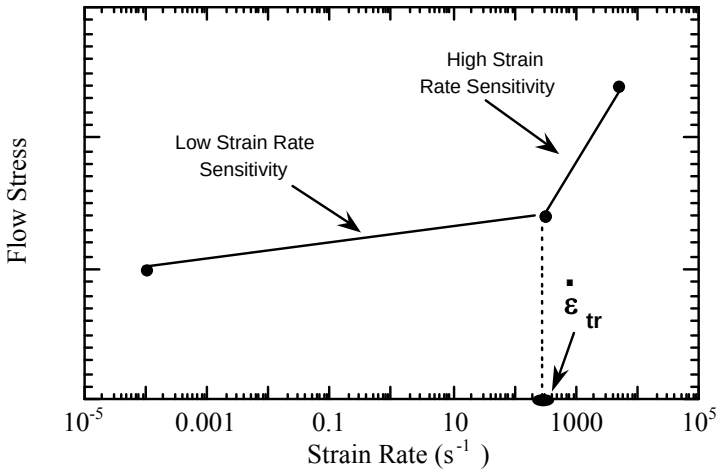

Figure 6.1. Schematic of the flow stress (constant strain) variation with strain rate in metallic materials [31].

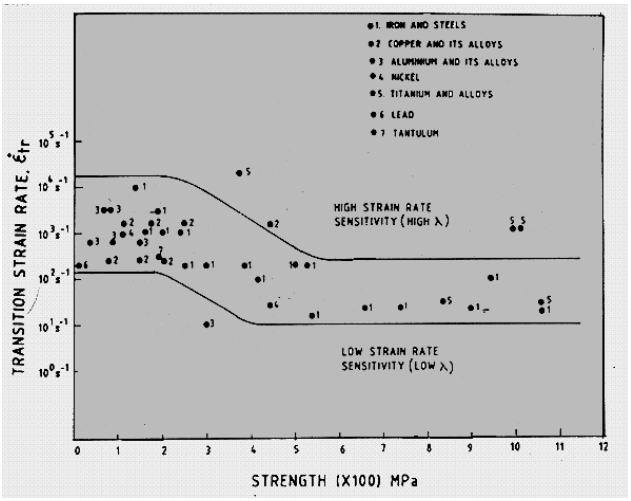

Figure 6.2. Transition strain rate *vs.* strength for common metals and alloys [32].

6.2.2. Composite Stress-Strain Curve and Rate Sensitivity

The agreement between the unit cell model and experimental stress-strain curves for the 15% particle reinforced MMCs is reasonably good, although the latter shows slightly higher flow stresses before 15% strain (Figure 5.14). At lower strains, below 5%, high strain rate flow stress data of SHPB testing however do not show exact material property. This is because at least four stress wave reversals are required in SHPB for stress homogenization in the sample, which may occur approximately within 1-4 microseconds (0-10% strain) depending on tested sample wave velocity and size and applied strain rate. At lower strain rates and for small size samples, stress homogenization occurs at lower strain levels. One can therefore tends to use flow stresses obtained at lower strain rates for the representative material property. However, the lower the strain rate is, the smaller the final strain attained is in the sample and therefore; comparison of the relatively lower and higher strain rate flow stresses at larger strain levels is not possible.

It is noted that while numerical flow stresses increase continuously with increasing strain, the experimental quasi-static and high strain rate flow stress started to decrease after 15% strain. This is most likely due to the damage accumulation in the composite and at larger strains, about 30% strain, the composite failed by forming shear bands, lining 45 degrees to the load axis as shown in Figure 6.3 for a sample tested until about 30% strain. When damage accumulation rate in the composite becomes higher than strain hardening rate, a decline in strength emerges and finally material fails. The continuous increase of stress and strain levels in the composite would eventually induce

damages in the composite particularly in particle-matrix interface, particle and matrix. Interface debonding and particle and matrix cracking, leading to the reduction of the strength, have been previously observed in particulate reinforced MMCs [1].

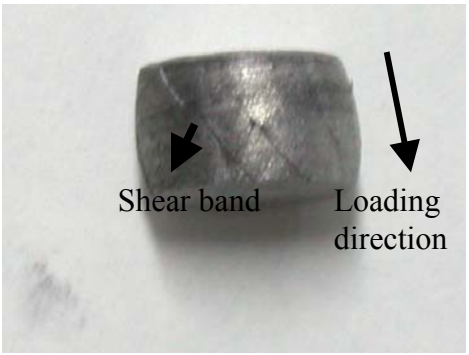

Figure 6.3. Quasi-statically deformed composite sample, showing shear bands on the surface.

Increasing particle volume fraction has been found to have two major effects on the composite stress-strain behavior (Figure 5.5). These are i) increase of the flow stress and b) strain hardening rate. An increase in the volume fraction of the particle obviously increases the amount of load carried by the strong particles. The higher strain hardening behavior of the composite with the higher particle volume fractions is due to the development of the higher stresses as compared with the composite with lower particle volume fraction at the same average strain.

The increased strain sensitivity of the composite relative to the matrix alloy is due to the constraint effect of the particles [7,10]. This effect also increases with increasing particle volume fraction. The higher the particle volume fraction, the larger the maximum strain and hence the strain rate attained in the composite, leading to increased strain rate sensitivity. At an average strain rate, for example, the maximum strain rate in the matrix may rise well above the average strain rate. This forms a strengthening effect in the composite if the matrix flow stress is strain rate sensitive. Li and Ramesh [7] have previously proposed this explanation for the increased strain rate sensitivity in the particle reinforced MMCs. The model developed in this study, however, is based on the deformation of the composite with a matrix material whose constitutive equation is known. Since the matrix flow stress increases with increasing strain rate, the composite flow stress also increases but with an amount higher than the matrix flow stress at a constant strain. Therefore, the proposed model requires the use of

the matrix constitutive equations which is available for the majority of the Al alloys and most of the Al alloys have been found to have strain rate sensitive flow stress behavior as depicted in Figure 6.4, in which the strain rate sensitivity parameter was drawn as a function of flow stress at 1 s^{-1} for common Al-alloys.

The increased rate sensitivity of the composite in the constrained model as compared with the unconstrained model is due to particle constraint effect. This is clearly seen in Figure 5.2, where constrained model induces higher stresses than the unconstrained model at the same average strain.

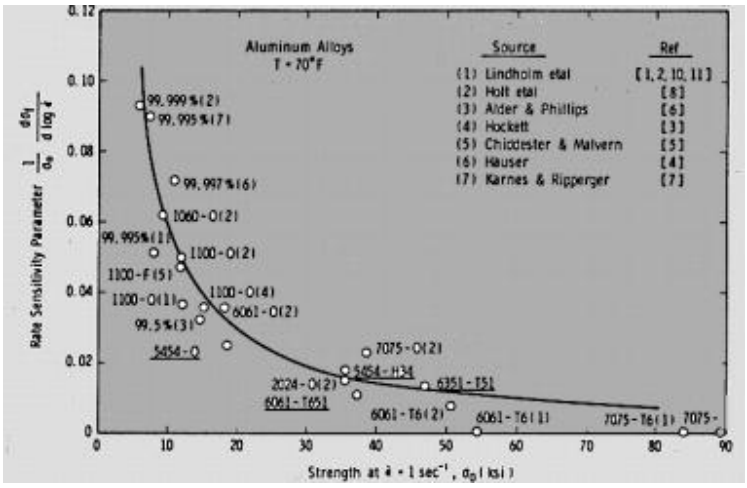

Figure 6.4. Rate sensitivity parameter *vs.* strength ($\dot{\varepsilon}$=1s^{-1}) of Al and its alloys [44].

The rate insensitive behavior of the ceramic materials has been observed in the strain rate regime of quasi-static to 100s s^{-1} [34]. Strain rate sensitive failure strength in ceramic materials has been found at strain rates higher than 1000 s^{-1} [34]. However such high strain rates could only be attained in the composite when the average strain rate in the composite would reach extremely high strain rates. The validity of the assumption of rate insensitive particle stress is also shown in Figure 5.20; the strain and hence strain rate on the particle is much smaller than the average strain.

The discrepancy between experimental and numerical flow stresses and rate sensitivities of the composite might be due to several complex factors, which will be elaborated below.

One reason of the discrepancy may be due to the experimental errors in the SHPB as explained previously. The errors in SHPB analysis mostly occur at low strains and therefore; could not be used to explain for the discrepancies at larger strains.

One should also consider the fact that the matrix macrostructure in the composite might be quite different from that in monolithic alloy, although both have the same alloy composition. Microscopic studies have shown that, in particulate reinforced MMCs, the grain size is smaller than that in the monolithic matrix produced by the same processing parameters [35]. The precipitation reactions were also faster in the composite [35]. Therefore, the microstructure of the matrix may be enhanced by the present particles. Moreover, the difference in thermal expansion coefficients of the Al and SiC results in development of residual stresses in the composite. Residual stresses are likely to increase flow stress in compression because in the studied particular composite system, the matrix might be under the tensional residual stresses. These tend to increase the flow stresses of the composite. It was shown that alloying and heat treatment processes applied to Al reduced the strain rate sensitivity relative to the pure Al.

In metals, most of the plastic deformation work is converted into heat and the conversion factor is usually assumed around 90-95% [36]. Mason *et al.* [37] measured the rate of conversion of plastic work into heat in 2024 Al alloy at high strain rates. The conversion factor was found to reach 85-90% after about 10% strain, a result that is very similar to the predicted value of this conversion factor. At high strain rates, the deformation is usually assumed to be adiabatic or near to the adiabatic condition due to short deformation duration for any significant heat dissipation [38,39]. Under adiabatic conditions, the temperature of the material increases as deformation proceeds and the increase of temperature is calculated using

$$\Delta T = \frac{\psi}{C\rho}\int \sigma d\varepsilon \qquad (6.3)$$

where ΔT, C and ρ are the temperature increase, specific heat and density, respectively and ψ is the conversion factor of plastic work into heat (usually taken as 0.9). The flow stress of most metals is quite sensitive to temperature [40] and, therefore, adiabatic heating can cause stress softening. The effect of stress softening due to adiabatic heating should be also taken into account for particularly strain rates above 100 s^{-1}. The critical strain rate for adiabatic strain rates is given as [41]

$$\varepsilon_{cr} = \frac{4\alpha\varepsilon}{L^2} \tag{6.4}$$

where α is the thermal diffusivity and L is the specimen length. Using a thermal diffusivity of $5x10^{-5}$ m^2s^{-1} for Al, initial specimen length of 10 mm and a strain of 20%, the critical strain rate is found to be ~0.4 s^{-1}. One can therefore consider all the quasi-static tests of the composite as isothermal and high strain rate tests as adiabatic. Since the thermal diffusivity of the composite is lower than the monolithic alloy, lower critical strain rates for the adiabatic heating of the composite is predicted. Using Equation 6.3, the isothermal stress-strain curves of the composite (%15) and matrix material is calculated according to the equation

$$\sigma_{\text{isothermal}} = \sigma_{\text{adiabatic}} + \frac{\partial\sigma}{\partial T}\Delta T \tag{6.5}$$

where $\partial\sigma/\partial T$ is the thermal softening parameter. Following parameters are further used in calculations: Thermal softening parameter; 0.5 MPa ^oC and heat capacity; 875 for 2024 and 843 for the SiC MMC. The calculated isothermal curves for the composite and 2024-O are shown in Figure 6.5. At 5, 10 and 15% strains the increase of stress due to adiabatic heating for 2024 and composite are 2, 4.5 and 7 MPa and 3, 7.3 and 11 MPa respectively. Although utilization of isothermal stress-strain curves increases the rate sensitivity parameter of the composite, the discrepancy between experimental and numerical strain rate sensitivity parameters are still relatively large. It is also noted that the difference between experimental and numerical stress-strain curves increases further with isothermal stress-strain curve as shown in Figure 6.6.

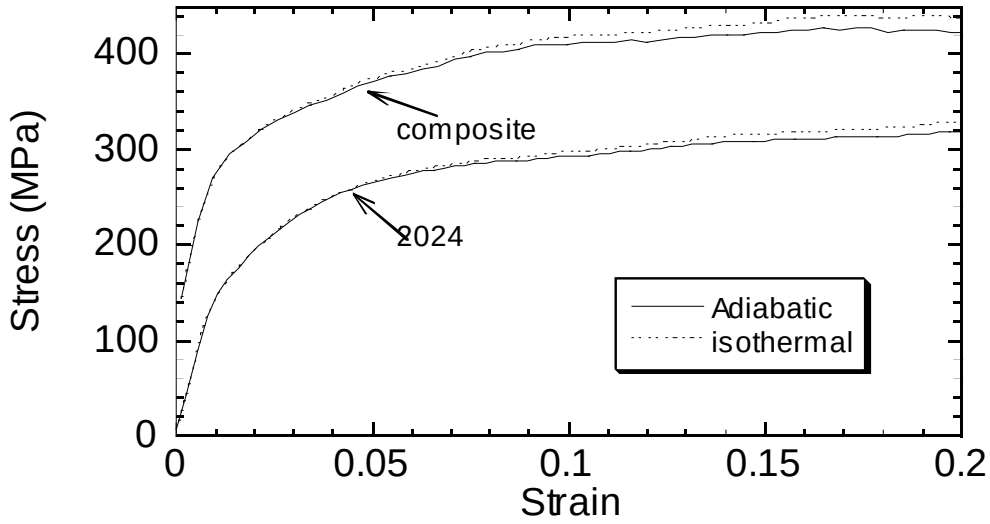

Figure 6.5. Isothermal curves for the composite and 2024-O

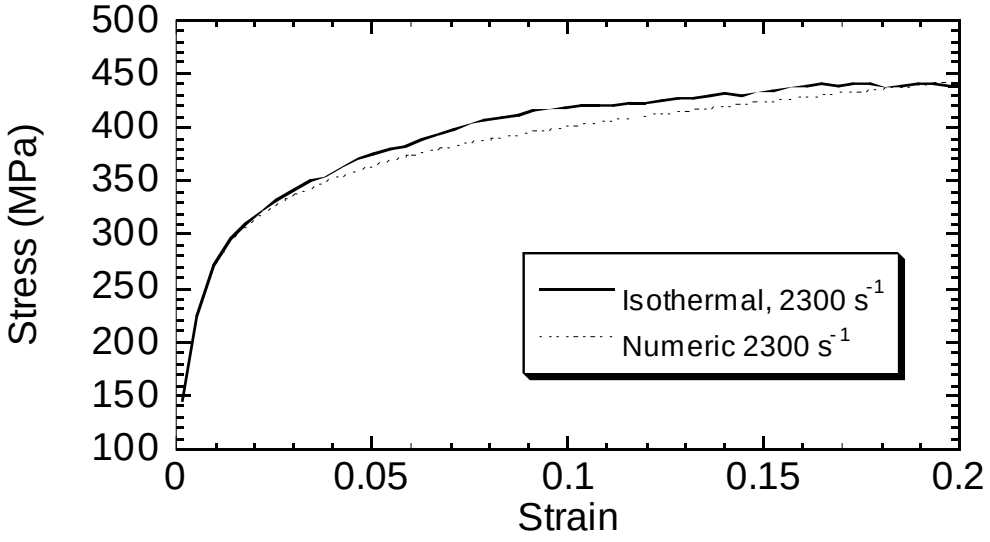

Figure 6.6. Experimental and numeric stress-strain curves of MMC.

It has been found that particles that have sharp corners have higher strengthening effect in the composite than spherical particles [24]. A similar result was also found in this study as depicted in Figure 5.28. The lower ductility and higher flow stress in short fiber reinforced MMCs as compared with particulate reinforced MMCs are simply due to the fact that higher local stresses are developed in these composites. The SiCp in the studied composite is not really spherical but have an irregular shape

with sharp corners. Real composite particles are also not perfectly cylindrical in shape. The stress-strain curve would therefore be in between spherical and cylindrical case, but biased towards the spherical case.

Previous numerical study has shown that particle-clustering increases the plastic strains accumulated in the matrix, leading to a higher strain hardening and thus a higher flow stress [42]. Although the effect of particle-clustering on the strain rate sensitivity has not been investigated yet, the development of higher plastic strains is expected to increase constraint effect of the particles, which may lead to higher strain rate sensitivity.

During processing of the composite, the SiC particles may react with liquid Al, producing brittle Al-C phase and Si-rich region around the particle. The Al-C phase is extremely brittle and it cannot be resolved under the electron microscope. The effect of brittle interface on the strain rate sensitivity is however not known very well.

The damage accumulation in the composite with increasing strain reduces degradation in the flow stresses of the composite. The reflections of stress waves at the boundaries could form complex wave interactions and result in rise of the damage accumulation rate.

As a summary, several parameters are considered for the discrepancy between experimental and numerical results. Among them, enhancement of the composite matrix microstructure, thermal residual stresses, sharp corners and clustering of particles tend to increase flow stresses of the composite, while adiabatic heating and damage accumulation tend to decrease flow stress. The parameters that affect the strain rate sensitivity of the composite however should be further investigated through a systematical experimental research program that provides large number of data on composites of varying particle volume fractions and matrix alloys.

Present model can be used to predict both small and large strain deformation behavior of the composite by applying suitable displacement increments. Not only particle reinforced composite's but also short and long fiber reinforced composite's mechanical behavior can be modeled by adapting suitable reinforcement shape and entering appropriate material properties.

CHAPTER 7

CONCLUSIONS

Strain rate dependent compression mechanical behavior of a SiC-particulate reinforced Al (2024-O) MMC with different particle volume fractions has been numerically investigated. An axisymmetric Finite Element unit cell model in which an elastic particle is embedded inside a strain rate sensitive visco-plastic matrix was used to determine composite stress-strain curves at various strain rates. The numerically calculated and experimentally found stress-strain curves and strain rate sensitivities were also compared for 15% particulate reinforced MMC. The followings have been found based on numerical and experimental results:

1. The average flow stresses of the MMC increase with increasing reinforcement volume fraction. A higher strain hardening rate behavior was also found in the composite as compared with matrix alloy.
2. The strain rate sensitivity of the composite was higher than that of the matrix. Strain rate sensitivity of the composite was further found to increase with increasing strain although the matrix strain rate sensitivity was constant. This was attributed to the constrained effect of the particles.
3. Strain rate sensitivity of the composite increased with the increasing particle volume fraction at the same particle size. This was again attributed to the increased constrained effect of the particles with increasing particle volume fraction.
4. Relatively good correlation between experimental and numerical stress-strain curves of the composite was found at strains less than 15%. The discrepancy at larger strains was attributed to damage accumulation.
5. Although experimental strain rate sensitivity of 15% SiC reinforced MMC, increased with increasing strain, it was found to be smaller than the numerical values. Several reasons for the discrepancy were discussed including adiabatic heating, microstructural variations between the composite matrix and matrix alloy, particle shape and distribution and damage accumulation.

6. It was found that the constrained model resulted in higher stresses as compared with the unconstrained model. This was likely due to the development of internal stresses for the geometrical fit arising from the constraint.
7. It was also confirmed in this study that cylindrical particles induce higher average and local stresses in the composite as compared with spherical particles.

REFERENCES

[1] T. W. CLYNE, P. J. WITHERS, "An Introduction to Metal Matrix Composites", *Cambridge University Press*, 1993.

[2] M. Güden, I. W. Hall, "Quasi-static and dynamic compression behaviour of an FP™ alumina-reinforced aluminium metal matrix composite", *Journal of Material Science* **33** (1998) 3285-3291.

[3] A.G. Evans, J. W. Hutchinson, R. M. McMeeking, "Stress-strain behavior of metal matrix composites with discontinuous reinforcements", *Scripta Metallurgica et Materialia,* **25**, pp. 3-8, 1991.

[4] J. Yang, S. M. Pıckard, C. Cady, A. G. Evans, R. Mehrabbbıan, "The stress/strain behavior of aluminum matrix composites with discontinuous reinforcements", *Acta metal. Mater.* **39**, No. 8. Pp. 1863-1869, 1991.

[5] W. Tong, G. Ravichandran, "Effective elastic moduli and characterization of a particulate metal-matrix composite with damaged particles", *Composites Science and Technology*, **52** (1994) 247-252.

[6] M. Dong, S. Schmauder, T. Bidlingmaier, A. Wanner, "Prediction of the mechanical behaviour of short fiber reinforced MMCs by combined cell models", *Computational Materials Science*, **9** (1997) 121-133.

[7] Y. Li, K.T. Ramesh, E.S.C. Chin, "The compressive viscoplastic response of an A359/SiCp metal-matrix composite and of the A359 aluminum alloy matrix", *International Journal of Solids and Structures,* **37** (2000) 7547-7562.

[8] A. F. Whitehouse, T. W. Clyne, "Critical Stress Criteria for Interfacial Cavitation in MMCs", *Acta metal. Mater*., **43**. No. 5. pp. 2107-2114. 1995.

[9] Yoshihiro Tomita, Yoshikazu Higa, Takehiro Fujimoto, "Modeling and estimation of deformation behavior of particle-reinforced metal-matrix composite", *International Journal of Mechanical Sciences*, **42** (2000) 2249-2260.

[10] G. Bao, Z. Lin, "High strain rate deformation in particle reinforced metal matrix composites", *Acta Mater*. **44**, no 3, pp. 1011-1019, 1996.

[11] G. Meijer, F. Ellyin, Z. Xia, "Aspect of residual thermal stress/strain in particle reinforced metal matrix composites", *Composites Part B; Engineering*, (2000) 29-37.

[12] T. Christman, A. Needleman, S. Nutt, S. Suresh, "On microstructural evolution and micromechanical modeling of deformation of a whisker-reinforced metal-matrix composite", *Material Science and Engineering*, **A107** (1989) 49-61.

[13] Harding, J. et al., in Proc. 6th Int. Conf. On Composite Materials (ICCM VI), Vol. **3**, ed. F. L. Matthews et al. *Elsevier Applied Science*, London, 1987, pp. 76-85.

[14] Marchand, A. et al*., Engng Fract. Mech*., 1988, **30**, 295.

[15] Perng, C. C.et al., *Mater. Sci. Engng A*, 1993, **171**, 213.

[16] Hong, S. I. and Gray, G. T. III, *J. Mater. Sci*., 1994, **29**, 2987.

[17] Mukai, T., et al., in Metallurgical and Materials Applications of Shock-Wave and High-Strain-Rate Phenomena, ed. L. E. Murr, K. P. Staudhammer and M. A. Meyers. *Elsevier*, Amsterdam, 1995, pp. 885-891.

[18] S. Yadav, D. R. Chichili, K. T. Ramesh, "The mechanical response of a 6061-t6 Al/Al_2O_3 metal matrix composite at high rates of deformation*", Acta metall.mater*. **43**, no 12, pp. 4453-4464, 1995.

[19] Chichili, D. R. and Ramesh, K. T., Int. *J. Solids Struct*., 1995, **32**(17/18), 2609.

[20] Vaidya, R. U., et al., in Shock Compression of Condensed Matter 1995, ed. S. C. Schmidt and W. C. Tao. *American Institute of Physics*, Woodbury, New York, 1996, pp. 643-646.

[21] Gray, G. T., III, et al., in Shock Compression of Condensed Matter 1995, ed. S. C. Schmidt and W. C. Tao. *American Institute of Physics*, Woodbury, New York, 1996, pp. 547-550.

[22] Mustafa Güden, High Strain Rate Behavior of Metal Matrix Composites*, PhD Thesis Technical Report*, University of Delaware, December 1997

[23] Yadav, S., An experimental and numerical investigation of dynamic deformations in metal-matrix and tungsten-based composites. *Ph.D. dissertation*, The Johns Hopkins University, 1996.

[24] C. R. Chen, S. Y. Qin, S. X. Li, J. L. Wen, "Finite element analysis about effects of particle morphology on mechanical response of composites", *Materials Science and Engineering A* **278** (2000) 96-105

[25] R. R. Irving, Iron age, **226** (1983) 35.

[26] A. Mortensen, J. Cornie and M. C. Flemings, *J. Metal*., **Feb.** (1988) 12.

[27] C. Ponzi, *Comp. Manuf*., **1** (1992) 32.

[28] H. L. Cox, "The elasticity and strength of paper and other fibrous materials", *Brit. J. Appl. Phys.* **3**, (1952) pp. 73-79.

[29] *LUSAS Modeller User Manual*, Version 13, 1999.

[30] *LUSAS Theory Manual 1*, Version 13, 1999

[31] Y. Tirupataiah and G. Sundararajan, *Mater. Sci. Eng*., **A189** (1994) 117.

[32] Y. Tirupataiah, *Ph.D. Thesis*, Banaras Hindu University, India, 1991.

[33] W. G. Ferguson, A. Kumar and J. E. Dorn, *J. Appl. Phys*., **38** (1967) 1836.

[34] James Lankford, "Dynamic compressive fracture in fiber-reinforced ceramic matrix composite", *Materials Science and Engineering*, **A107**, 261-268, (1989).

[35] F. J. Humpherys, in: 9th. RiseInt. Symp. Mater. Sci., N. Andersen et al. (Edts), Riso National Lab., Roskilde, denmark, (1988), 51.

[36] H. C. Rogers, Material Behavior Under High Stress and Ultrahigh Loading Rates, J. Mescall and V. Weiss (Edts.), *Plenium Press*, New York, (1983) 101.

[37] J. J. Mason, A. J. Rosakis and G. Ravichandran, *Mech. Mater*., **17** (1994) 135.

[38] H. C. Rogers, Adiabatic Shearing- *A Review. Drexel Univ. Rep*., (1974) 73.

[39] H. C. Rogers, *Ann. Rev. Mat. Sci*., **9** (1979) 283.

[40] C. Zener and J. H. Hollomon, *J. Appl. Phys*., **15** (1944) 22.

[41] M. A. Meyers, G. Subhash, B. K. Kad, L. Prasad, *Mech. Mater*., **17** (1994) 175.

[42] A. Borley, H. Biermann, O. Hartmann, "FE investigation of the effect of particle distribution on the uniaxial stress-strain behavior of particulate reinforced metal-matrix composite", *Materials Science and Engineering*, **A313**, 34-45, (2001).

[43] *ANSYS Training Manual*.

[44] U. S. Lindholm, R. L. Bessey and G. V. Smith, *J. Mater*., IMLSA, **6**, (1971), 119.

APPENDIX 1

LUSAS Finite Element System

A complete finite element analysis involves three stages.

- Pre-Processing
- Finite Element Solver
- Results-Processing

The LUSAS Finite Element System consists of two parts to perform a full analysis:

- LUSAS Modeller is a fully interactive pre- and post-processing graphical user interface.
- LUSAS Solver performs the Finite Element Analysis.

Pre-Processing

Pre-processing involves creating a geometric representation of the structure, then assigning properties, then outputting the information as a formatted data file (.dat) suitable for processing by LUSAS.

Creating a Model

A model is a graphical representation consisting of Geometry (Points, Lines, Combined Lines, Surfaces and Volumes) and Attributes (Materials, Loading, Supports, Mesh, etc.). Each part of the model is created in two steps:

- Define the Feature or Attribute.
- Assign the Attribute or Attributes.

Features can be defined by entering coordinates, selecting Points on the screen or by using utilities such as transformations. An attribute is first defined by creating an attribute dataset. The dataset is then assigned to chosen features. For example, to assign a Point Load (Attribute) to a Point (Feature) representing the corner of a platform.

To complete a model it may be necessary to define additional utilities called control datasets. These are used to control the progress of advanced analyses.

Finite Element Solver

Once a model has been created by clicking on the solve button the solution stage begins. LUSAS creates a data file from the model, solves the stiffness matrix, and

produces a results file (.mys). The results file will contain some or all of the following data:

Stresses · Strains · Displacements · Velocities
· Accelerations · Residuals · Reactions · Yield flags · Potentials
· Fluxes · Gradients · Named variables · Combination datasets
· Envelope definitions · Fatigue datasets · Strain energy

Results-Processing

Results-processing involves using a selection of tools for viewing and analysing the results file produced by the Solver. Many different ways of viewing results are supported:

- Contour plots (averaged/smoothed)
- Contour plots (unaveraged/unsmoothed)
- Undeformed/Deformed Mesh Plots
- Wood-Armer Reinforcement Calculations
- Animated Display of Modes/Load Increments
- Section Line/Slice Plots
- Yield Flag Plots
- Graph Plotting
- Vector Plots

Input Parameters

1.Control parameters

1.Number of Elements

2.Number of Nodes

3.Number of B.C.'s

4.Number of Nonzero Forces

2.Geometry

1.x,y,z location of each node

2.Element connectivity (which nodes are associated with which elements)

3.Element Properties

1.Area

2.Moment of Inertia

3.Thickness

4.Location of Neutral Axis

4.Loading Information

1.Location and magnitude of every external force.

2.Location and magnitude of every constrained d-o-f

APPENDIX 2

Axisymmetric solid element properties

General

Element Name: TAX3 TAX6 QAX4 QAX8

Element Group: 2D Continuum

Element Subgroup: Axisymmetric Solid

Element Description: A family of 2D isoparametric elements with higher order models capable of modelling curved boundaries. The formulations apply over a unit radian segment of the structure and the loading and boundary conditions are axisymmetric. By default, the Y-axis is taken as the axis of symmetry. The elements are numerically integrated.

Number Of Nodes: 3, 4, 6, or 8 numbered anticlockwise.

Freedoms **U, V:** at each node.

Node Coordinates **X, Y:** at each node.

Geometric Properties

Not applicable (a unit radian segment is assumed).

Material Properties

Linear

Isotropic: MATERIAL PROPERTIES (Elastic: Isotropic)

Orthotropic: MATERIAL PROPERTIES ORTHOTROPIC AXISYMMETRIC (Elastic: orthotropic Axisymmetric)

Anisotropic: MATERIAL PROPERTIES ANISOTROPIC 4 (Not supported in LUSAS Modeller)

Rigidities: Not applicable.

Matrix: Not applicable.

Joint: Not applicable.

Concrete: MATERIAL PROPERTIES NONLINEAR 82 (Elastic: Isotropic, Plastic: Cracking concrete)

Elasto-Plastic

Stress resultant: Not applicable.

Tresca: MATERIAL PROPERTIES NONLINEAR 61 (Elastic: Isotropic, Plastic: Tresca, Hardening: Isotropic Hardening Gradient, Isotropic Plastic Strain or Isotropic Total Strain)

Drucker-Prager: MATERIAL PROPERTIES NONLINEAR 64 (Elastic: Isotropic, Plastic: Drucker-Prager, Hardening: Granular)

Mohr-Coulomb: MATERIAL PROPERTIES NONLINEAR 65 (Elastic: Isotropic, Plastic: Mohr-Coulomb, Hardening: Granular with Dilation)

Von Mises (B/Euler): MATERIAL PROPERTIES NONLINEAR 75 (Elastic: Isotropic, Plastic: Von Mises, Hardening: Kinematic)

Volumetric Crushing: MATERIAL PROPERTIES NONLINEAR 81 (Volumetric Crushing or Crushable Foam)

Rubber: Not applicable.

Composite: Not applicable.

Field: Not applicable.

Stress Potential: STRESS POTENTIAL VON_MISES, HILL, HOFFMAN

Creep: CREEP PROPERTIES (Creep)

Damage: DAMAGE PROPERTIES SIMO, OLIVER (Damage)

Viscoelastic: VISCO ELASTIC PROPERTIES

Loading

Prescribed Value PDSP, TPDSP Prescribed variable. U, V: at nodes.

Concentrated Loads CL Concentrated loads. Px, Py: force per unit radian at nodes.

Element Loads Not applicable.

Distributed Loads UDL Not available.

FLD Face loads. Px, Py: local face pressures at nodes (force per unit area).

Body Forces CBF Constant body forces for element. Xcbf, Ycbf, Wx, Wy (angular velocity must be applied about axis of symmetry)

BFP, BFPE Body force potentials at nodes/for element. 0, 0, 0, j4, Xcbf, Ycbf

Velocities VELO Velocities. Vx, Vy: at nodes.

Accelerations ACCE Acceleration Ax, Ay: at nodes.

InitialStress/Strains SSI, SSIE Initial stresses/strains at nodes/for element. sx, sy, sxy, sz: global stresses. ex, ey, gxy, ez: global strains.

SSIG Initial stresses/strains at Gauss points. sx, sy, sxy, sz: global stresses. ex, ey, gxy, ez: global strains.

ResidualStresses SSR, SSRE Residual stresses at nodes/for element. sx, sy, sxy, sz: global stresses.

SSRG Residual stresses at Gauss points. sx, sy, sxy, sz: global stresses.

Temperatures TEMP, TMPE Temperatures at nodes/for element. T, 0, 0, 0, To, 0, 0, 0

Field Loads Not applicable.

TempDependentLoads Not applicable.

Output

LUSAS Solver Stress (default): sx, sy, sxy, sz, smax, smin, b, ss, se (see description of principal stresses)

Strain: ex, ey, gxy, ez, emax, emin, b, es, ee

LUSAS Modeller See Results Tables (Appendix K).

Local Axes

Not applicable (global axes are the reference).

Sign Convention

· Standard 2D continuum element

Formulation

Geometric Nonlinearity

Total Lagrangian For large displacements and large rotations.

Updated Lagrangian For large displacements and large rotations.

Eulerian For large displacements, large rotations and moderately large strains.

Co-rotational Not applicable.

Integration Schemes

Stiffness Default. 1-point (TAX3), 3-point (TAX6), 2x2 (QAX4, QAX8)

Fine (see Options). 3x3 (QAX8), 3-point (TAX3).

Mass Default. 1-point (TAX3), 3-point (TAX6), 2x2 (QAX4, QAX8)

Fine (see Options). 3x3 (QAX8), 3-point (TAX3).

Mass Modelling

Consistent mass (default).

Lumped mass.

Options

18 Invokes finer integration rule.

47 X-axis taken as axis of symmetry.

54 Updated Lagrangian geometric nonlinearity.

55 Output strains as well as stresses.

87 Total Lagrangian geometric nonlinearity.

91 Invokes fine integration rule for mass matrix.

105 Lumped mass matrix.

123 Clockwise node numbering.

139 Output yielded Gauss points only.

167 Eulerian geometric nonlinearity.

Notes on Use

1 The element formulations are based on the standard isoparametric approach. The variation of stresses within an element can be regarded as constant for the lower order (corner node only) elements, and linear for the higher order (mid-side node) elements.

2 All elements pass the patch test.

3 Non-conservative loading is available with these elements when using either Updated Lagrangian or Eulerian geometric nonlinear formulations together with the FLD loading facility.

4 Option 123 will not operate on a mesh with a mixture of clockwise and anti-clockwise elements, it is only applicable if every element is numbered clockwise. Surface normals should be visualised and if necessary corrected in the pre-processing stage.

Using Option 123 with local loading types, such as FLD and UDL, will cause load reversal.

5 The maximum and minimum principal stress computations for axisymmetric elements do not include the sz term as this is implicitly a principal stress in a biaxial stress field.

Restrictions

- Ensure mid-side node centrality
- Avoid excessive element curvature
- Avoid excessive aspect ratio

Recommendation on Usage

The 8-noded element with a 2*2 Gauss rule is usually the most effective element, as the under-integration of the stiffness matrix prevents locking, which may occur either when the element is subjected to parasitic shear, or as the material reaches the incompressible limit (elasto-plasticity). The Gauss point stresses are also sampled at the most accurate locations for the element. However, the element does possess one spurious zero energy mode. This mode is very rarely activated in linear analysis, but it may occur in both materially and geometrically nonlinear analyses. Therefore, a careful examination of the solution should be performed, to check for spurious stress oscillations and peculiarities in the deformed configuration.

The 8-noded element with a 3*3 Gauss rule may be used if a spurious mechanism is excited with the 2*2 Gauss rule.

The 4-noded element should not be used for analyses where in-plane bending effects are significant as the element tends to lock in parasitic shear.